

Banner appropriate to article type will appear here in typeset article

1 Self-similarity and growth of non-linear magnetic 2 Rayleigh-Taylor instability - Role of the magnetic 3 field strength

4 Manohar Teja Kalluri[†], Andrew Hillier

5 Department of Mathematics and Statistics, University of Exeter, Exeter, United Kingdom

6 (Received xx; revised xx; accepted xx)

The non-linear regime of the magnetic Rayleigh-Taylor instability (MRTI) plays a crucial role in the transportation and mixing of material in a wide range of laboratory to astrophysical systems. But several fundamental aspects of this regime remain poorly understood. Previous MRTI studies assumed MRTI to have a self-similar, quadratic growth in the non-linear regime, similar to the hydrodynamic (HD) RTI. However, neither the self-similarity nor the relevance of the HD scaling for the MRTI has been proved analytically. Further, the role of magnetic field on the evolution of the instability remain unexplored. Towards this, we perform analytical and numerical study of the MRTI with uniform magnetic field. Our study reveals that the imposed magnetic field deviates the MRTI evolution from self-similarity. However, the HD RTI scaling becomes relevant to the MRTI evolution when the non-linear dynamics dominate the imposed magnetic field. A formula for the α_{mhd} , a quantity which represents the non-linear growth of instability in the self-similar regime, was obtained. The formula of α_{mhd} highlight the physical processes that could dictate the growth of instability. Numerical simulations of the MRTI showed the quantitative variation of these physical processes and α_{mhd} across a wide range of magnetic field strengths. Thus, the current study proves, analytically and numerically, the role of magnetic fields on the evolution of MRTI and the factors that influence of non-linear growth constant of the instability.

Key words:

1. Introduction

When a low density fluid is supporting a high density fluid in the presence of gravity, perturbations at the interface of the two fluids could lead to the penetration of one fluid into the other. This phenomenon is called the Rayleigh-Taylor instability (RTI). The region of the penetration or the mixing of the two fluids is called the mixing layer. A special case of the instability evolution in the presence of magnetic fields, is called the magnetic Rayleigh-Taylor instability (MRTI). The MRTI is known to occur in a wide range of systems like inertial confinement fusion (Zhang *et al.* 2018; Srinivasan *et al.* 2012), Earth's ionosphere

[†] Email address for correspondence: manohartejakalluri25@gmail.com

(Ott 1978; Keskinen *et al.* 1981), quiescent solar prominence (Hillier 2018), accretion discs (Kulkarni & Romanova 2008; Zhdankin *et al.* 2023), and nebula (Hester *et al.* 1996). The MRTI mixing layer is the region of various interesting turbulent dynamics like the fluid mixing, and transportation, for example mixing of prominence and corona material in the solar atmosphere (Hillier 2018), transportation of stellar material into the surrounding medium in supernova (Fraschetti, F. *et al.* 2010), accretion of material on to the central object in accretion discs (Kulkarni & Romanova 2008). The growth and the dynamics of the mixing layer are hence topics of great interest. However the evolution of the MRTI remains poorly understood.

Before we address the evolution of RTI in the presence of magnetic field, let us review the foundational case of evolution of RTI in the absence of magnetic field, called the hydrodynamic (HD) RTI. In the HDRTI, an infinitesimal perturbation at the interface leads to interpenetration of fluids, and mixing (Strutt 2009; Taylor 1950). In the early phase of evolution, the linear phase, the height of the mixing layer (h) is known to grow exponentially with time (t), $h \propto e^{\sigma t}$, at a growth rate $\sigma = \sqrt{Ak g}$ (Taylor 1950). Here, g is the acceleration due to gravity, k is the perturbation wave mode, and the Atwood number (A) represents the non-dimensionalized density difference between the two fluids, defined as $A = \frac{\rho_h - \rho_l}{\rho_h + \rho_l}$, where ρ_h and ρ_l are the densities of the high and low density fluids. Following the linear phase, in the non-linear phase, the height of the mixing layer was proved to grow quadratically in time as follows:

$$h = \alpha A g t^2 + 2\sqrt{\alpha A g h_0} t + h_0. \quad (1.1)$$

Here, α is the non-linear growth constant, and h_0 is the height of mixing layer at time $t=0$, assuming equation 1.1 is obeyed from $t=0$. The above equation was proved analytically and numerically (Ristorcelli & Clark 2004) in the Boussinesq limit, and was also verified experimentally at low density ratios (Dalziel *et al.* 1999; Linden & Redondo 1991). Following the dimensional analysis by Fermi & von Neumann (1953), it can be expected that the quadratic growth behaviour is valid for larger Atwood number cases too. The quadratic growth behaviour at large Atwood number was numerically reported by Youngs (1991); Dimonte *et al.* (2004). Thus, the mixing layer grows in a self-similar fashion ($h \propto A g t^2, t \gg 1$). α represents how fast the mixing layer grows, and hence determination of α is a problem of great interest. However, to our knowledge, no study explained the physical processes that effect the non-linear growth constant α . Typically, α is calculated from the slope of h and t^2 or $(\partial h / \partial t)^2$ and h . Numerous experimental and numerical studies of the HDRTI showed distinct α values, with a wide error range. These disagreements are well summarized in Glimm *et al.* (2001); Hillier (2020). Following several studies, α_b (α based on the bubble height h_b , which is the height of the top of the mixing layer from the center-line) for the HD case is expected to be between 0.03 and 0.08. Beyond the non-linear phase, mixing layer height saturates (i.e., $h \approx \text{constant}$) marking the onset of saturation phase. However, the system continues to undergo turbulent mixing until the gravitational potential energy, which drives the instability, is exhausted. Beyond this, the turbulence in the system starts to decay (Skoutnev *et al.* 2021).

Unlike the HD case, in the presence of magnetic field, RTI may not develop for every perturbation, specifically when the magnetic field and perturbations are non-perpendicular. This is due to the suppressing effect of the magnetic field on the instability in the linear regime (Chandrasekhar 1961). Assuming the flux frozen condition (perfect coupling of magnetic field lines and stream lines), when the magnetic field is non-perpendicular, the onset of the instability demands deformation of magnetic field lines. Thus, perturbations develop magnetic tension that resists the deformation of magnetic field lines, and the growth of instability. The stronger the magnetic field, the greater the suppression. This can be

understood from the linear growth rate (σ) equation (Chandrasekhar 1961),

$$\sigma = \sqrt{Akg - \frac{2k^2 B^2 \cos^2 \theta}{(\rho_h + \rho_l)}}, \quad (1.2)$$

where θ is the angle between \mathbf{k} and \mathbf{B} . From equation 1.2, the suppression effect is prominent on the wave modes parallel to the field ($\theta=0$, called undular modes), and the effect diminishes with increasing misalignment (θ). When the perturbations are perpendicular to the magnetic field ($\theta=\pi/2$, called interchange modes), the instability experiences no suppression. From equation 1.2, for a given A , g , θ and B , the growth rate decreases with increasing k . The value of k at which $\sigma = 0$ is called the critical wave number and is given by

$$k_c = \frac{(\rho_h - \rho_l)g}{2B^2 \cos^2 \theta}. \quad (1.3)$$

While the wave modes smaller than the k_c continue to grow, the modes larger than k_c are suppressed by the magnetic field. Thus the magnetic field selectively suppresses the perturbations.

This selective suppression has an important consequence in the non-linear MRTI. As we increase the magnetic field, the critical wave number decreases. That is only the large scale perturbations grow and the small scale perturbations are suppressed. This results in the mixing layer with laminar plumes at strong magnetic field strengths. Whereas at low magnetic field strengths, the mixing layer is relatively turbulent. The suppression of turbulence with increasing magnetic field strength was reported in numerous studies (Jun *et al.* 1995; Stone & Gardiner 2007b; Carlyle & Hillier 2017). Further, Stone & Gardiner (2007b) also reported that the introduction of magnetic field, however weak, enhances the non-linear growth constant with the magnetic field strength. This was based on the parametric study of MRTI where the α_{mhd} (calculated from $h \propto t^2$) increased from 0.021 to 0.034 with increasing magnetic field strength from HD to $60\%B_c$ (definition of B_c will be introduced in §3). They proposed that the suppression of secondary instabilities by the magnetic field lead to larger growth rates in the MRTI case. However, Carlyle & Hillier (2017) reported a decreasing trend of α (from 0.051 to 0.035) with increasing magnetic field strength (from $\approx 5\%$ to $\approx 12\%B_c$). In all the above studies, the magnetic field is imposed horizontally. Briard *et al.* (2022, 2024) showed that the vertical magnetic field produce elongated bubble and spikes.

A caveat of the non-linear MRTI studies so far is the assumption of quadratic growth (and self-similarity) of the mixing layer. However, unlike the HDRTI case, neither the self-similarity of MRTI, nor the quadratic growth of its mixing layer were rigorously proven. Such assumptions are also not obvious, in the light of suppressing effect magnetic fields had on the system, as seen from the growth rate of instability in the linear regime (equation 1.2). The quadratic growth of MRTI mixing layer height with time (similar to HDRTI) raises the question, what is the role of magnetic field on the evolution of the instability and its self-similar behaviour? Besides the disagreement on the trend of α with increasing magnetic field strength, we also lack an understanding on the factors that determine the α value.

Targeting the above questions, first an analytical analysis is performed to validate the self-similarity assumption and the appropriateness of HDRTI scaling for MRTI in § 2.1. The analysis also leads us to understand the role of magnetic field on the evolution characteristics of MRTI. Later, an analytical equation for the temporal growth of mixing layer in the self-similar regime was derived in § 2.2. The equation of mixing layer height leads us to an analytical formula for the non-linear growth constant, and towards understanding the factors

that control the growth of instability. Through the numerical simulations, we validate the conclusions from analytical study and gain a deeper understanding of MRTI dynamics, § 4.

2. Analytical proof of hydrodynamic self similarity in MRTI

2.1. The role of magnetic fields on self-similarity

Previous numerical studies of the non-linear MRTI reported that the mixing layer height grows quadratically with time (Jun *et al.* 1995; Stone & Gardiner 2007*b,a*; Carlyle & Hillier 2017). Following this, MRTI was assumed to have a self-similar evolution, with scaling laws similar to the HD case. However, an analytical proof of the self-similar evolution, and the relevance of HD scaling for the non-linear MRTI is still lacking. To verify this assumption, we perform an analytical self-similar analysis of the ideal MHD equations with the HD scaling.

Consider the system of ideal MHD equations given below.

$$\rho \partial_t \mathbf{U} + \rho (\mathbf{U} \cdot \nabla) \mathbf{U} = -\nabla p + (\mathbf{B} \cdot \nabla) \mathbf{B} - \delta \rho \mathbf{g}, \quad (2.1a)$$

$$\partial_t \mathbf{B} + (\mathbf{U} \cdot \nabla) \mathbf{B} = (\mathbf{B} \cdot \nabla) \mathbf{U}, \quad (2.1b)$$

$$\partial_t \rho + (\mathbf{U} \cdot \nabla) \rho = 0, \quad (2.1c)$$

$$\nabla \cdot \mathbf{U} = \nabla \cdot \mathbf{B} = 0. \quad (2.1d)$$

In the above equations, \mathbf{U} , \mathbf{B} , and ρ are the instantaneous velocity, magnetic field, and density, respectively. Gravity is assumed to act along the x_3 direction (i.e., $\mathbf{g}=(0, 0, -g)$). The high density fluid (ρ_h) is placed over the low density fluid (ρ_l) in the x_3 direction. Thus the MRTI grows along x_3 , which is the direction of statistical inhomogeneity. The other two directions x_1, x_2 are statistically homogeneous. p is the fluctuating pressure, $\delta \rho$ is the density fluctuations over initial density profile (ρ_0) ($\delta \rho = \rho - \rho_0$). In the current paper, vector variables are written in bold.

The flow variables \mathbf{U} and \mathbf{B} can be split into the initial and fluctuating components. The initial components are denoted with subscript 0. We consider the case of an initial stationary system (i.e., $\mathbf{U}_0=0$), and uniform magnetic field in x_1 direction, $\mathbf{B}_0=(B_0, 0, 0)$. The fluctuating components \mathbf{b} , \mathbf{u} , and $\delta \rho$ are three dimensional. For this case, equation 2.1 becomes:

$$\partial_t \rho u_i + \partial_j (\rho u_j u_i) = -\partial_i p + \partial_j (B_0 b_i) + \partial_j (b_j b_i) - \delta \rho g_i \delta_{i3}, \quad (2.2a)$$

$$\partial_t b_i + \partial_j (u_j b_i) = \partial_j (B_0 u_i) + \partial_j (b_j u_i), \quad (2.2b)$$

$$\partial_t \rho + \partial_j (u_j \rho) = 0, \quad (2.2c)$$

$$\partial_i u_i = \partial_i b_i = 0. \quad (2.2d)$$

where $i, j \in [1, 3]$, δ_{i3} represents the Kronecker delta function. From now on, ∂_j represent partial derivative with respect to x_j ($\partial_j = \frac{\partial}{\partial x_j}$), the Einstein summation rule is applicable everywhere. The above equations are obtained using the condition 2.2d. $\partial_j \mathbf{B}_0=0$ and $\partial_t \mathbf{B}_0=0$ as \mathbf{B}_0 is uniform and constant.

Since the aim is to validate the relevance of the HD scaling to the magnetohydrodynamic case, we non-dimensionalise the flow quantities in terms of the HD scaling. The density is non-dimensionalised using the arithmetic mean of ρ_h and ρ_l , denoted as ρ_m . From equation 1.1, we know that the mixing layer of HDRTI has a quadratic growth. The height of the HD mixing layer at late time can be approximated to $h \propto Agt^2$. The characteristic speed at the boundaries of the mixing layer is proportional to the temporal derivative of the mixing layer height, $u \propto \partial_t h \propto Agt$. Hence, we choose $Ag t$ as the characteristic speed (u_c) for non-dimensionalisation. From the definition of Alfvén velocity $v_A = B/\sqrt{\rho}$, the magnetic

field can be written in terms of velocity and density so we choose $u_c\sqrt{\rho_m}$ as the non-dimensional parameter for magnetic field. The pressure is non-dimensionalised as $\rho_m u_c^2$. The flow parameters can be written in non-dimensionalised forms as shown below:

$$\rho = \rho_m \tilde{\rho}, \quad u = Agt\tilde{u}, \quad b = \sqrt{\rho_m} Agt\tilde{b}, \quad p = \rho_m (Agt)^2 \tilde{p}.$$

Variables with tilde represent the non-dimensional forms of the corresponding variables. Rewriting the equations 2.2a, 2.2b, 2.2c in the non-dimensional form and averaging along the homogeneous directions $\left(\langle \star \rangle = \frac{1}{L_{x_1} L_{x_2}} \int_0^{L_{x_1}} \int_0^{L_{x_2}} \star dx_1 dx_2\right)$, we get

$$t\partial_t \langle \tilde{\rho} \tilde{u}_i \rangle + \langle \tilde{\rho} \tilde{u}_i \rangle + Agt^2 \partial_3 \langle (\tilde{\rho} \tilde{u}_3 \tilde{u}_i) \rangle + Agt^2 \partial_3 \langle \tilde{p} \rangle - Agt^2 \partial_3 \langle \tilde{b}_3 \tilde{b}_i \rangle + \frac{1}{A} \langle \tilde{\delta} \tilde{\rho} \tilde{\delta}_{i3} \rangle = 0, \quad (2.3a)$$

$$\partial_3 \langle \tilde{u}_3 \tilde{b}_i \rangle - \partial_3 \langle \tilde{b}_3 \tilde{u}_i \rangle = 0, \quad (2.3b)$$

$$\partial_t \langle \tilde{\rho} \rangle + Agt \partial_3 \langle \tilde{u}_3 \tilde{\rho} \rangle = 0. \quad (2.3c)$$

The above equations are obtained following the simplification $\partial_1 \langle \star \rangle = 0$, $\partial_2 \langle \star \rangle = 0$, since x_1 and x_2 are directions of statistical homogeneity.

The variables x_3 and t can be scaled to get a self similar variable $\xi = \sqrt{\frac{x_3}{Ag}} \frac{1}{t}$. The partial derivatives of x_3 and t can now be rewritten in terms of ξ as $\partial_t = \frac{-\xi}{t} \partial_\xi$, $\partial_3 = \frac{\xi}{2x_3} \partial_\xi$. The above system of equations modifies to

$$-d_\xi \langle \tilde{\rho} \tilde{u}_i \rangle + \langle \tilde{\rho} \tilde{u}_i \rangle + \frac{1}{2\xi} d_\xi \langle \tilde{\rho} \tilde{u}_3 \tilde{u}_i \rangle + \frac{1}{2\xi} d_\xi \langle \tilde{p} \rangle - \frac{1}{2\xi} d_\xi \langle \tilde{b}_3 \tilde{b}_i \rangle + \langle \frac{\tilde{\delta} \tilde{\rho} \tilde{\delta}_{i3}}{A} \rangle = 0, \quad (2.4a)$$

$$d_\xi \langle \tilde{u}_3 \tilde{b}_i \rangle - d_\xi \langle \tilde{b}_3 \tilde{u}_i \rangle = 0, \quad (2.4b)$$

$$\xi d_\xi \langle \tilde{\rho} \rangle + \frac{1}{2\xi} d_\xi \langle \tilde{u}_3 \tilde{\rho} \rangle = 0, \quad (2.4c)$$

where $d_\xi = \frac{d}{d\xi}$.

The solutions for the above ordinary differential equations (ODEs) are functions of ξ . Thus, momentum, density, and fluctuating magnetic field can take self-similar solutions similar to the HD scaling. However, the above quantities are not adequate to affirm the self-similar nature of the MRTI. An investigation into the higher order quantities like turbulent kinetic energy (TKE) is required (Baltzer & Livescu 2020; Rogers & Moser 1994). Hence, we investigate the self-similarity of the TKE and the turbulent magnetic energy (TME).

We defined the TKE and TME as $\frac{1}{2} \langle \rho u_i u_i \rangle$ and $\frac{1}{2} \langle b_i b_i \rangle$, respectively. To obtain the equation of TKE, we multiply equation 2.2a with u_i and average along homogeneous directions to get

$$\partial_t \left\langle \rho \frac{u_i u_i}{2} \right\rangle + \partial_3 \left\langle u_3 \rho \frac{u_i u_i}{2} \right\rangle + \partial_3 \langle u_3 p \rangle - B_0 \langle u_i \partial_1 b_i \rangle - \langle u_i b_j \partial_j b_i \rangle + \langle u_i \delta \rho g_i \delta_{i3} \rangle = 0. \quad (2.5)$$

In terms of non-dimensional quantities and self-similar variable, the equation 2.5 becomes

$$\begin{aligned} \langle \tilde{\rho} \tilde{u}_i \tilde{u}_i \rangle - \xi \partial_\xi \left\langle \tilde{\rho} \frac{\tilde{u}_i \tilde{u}_i}{2} \right\rangle + \frac{1}{2\xi} \partial_\xi \left\langle \tilde{u}_3 \tilde{\rho} \frac{\tilde{u}_i \tilde{u}_i}{2} \right\rangle - \frac{1}{2\xi} \partial_\xi \langle \tilde{u}_3 \tilde{p} \rangle - \frac{1}{2\sqrt{\rho_m} C \xi Agt} B_0 \langle \tilde{u}_i \partial_\xi \tilde{b}_i \rangle \\ - \frac{1}{2C\xi} \langle \tilde{u}_i \partial_\xi (\tilde{b}_1 \tilde{b}_i + \tilde{b}_2 \tilde{b}_i + C \tilde{b}_3 \tilde{b}_i) \rangle - \frac{1}{A} \langle \tilde{\delta} \tilde{\rho} \tilde{u}_i \tilde{\delta}_{i3} \rangle = 0, \end{aligned} \quad (2.6)$$

The ∂_1 , ∂_2 terms are written in terms of ∂_3 based on the scaling assumption $x_i = Cx_3$, $i = [1, 2]$. This assumption is based on the hypothesis that the flow structures evolve with a fixed scaling in each direction. In other words, the system has a fixed anisotropy during the self-similar phase. This assumption is verified later in § 4.2.3.

Similarly, the equation of TME is obtained by multiplying equation 2.2b with b_i , and the resultant equation is averaged along the homogeneous directions to get

$$\partial_t \left\langle \frac{b_i b_i}{2} \right\rangle + \partial_3 \left\langle u_3 \frac{b_i b_i}{2} \right\rangle - B_0 \partial_1 \langle b_i u_i \rangle + B_0 \langle u_i \partial_1 b_i \rangle - \langle b_j \partial_j (b_i u_i) \rangle + \langle u_i b_j \partial_j b_i \rangle = 0. \quad (2.7)$$

Writing the equation 2.7 in terms of non-dimensional variables and the self-similar variable, we get

$$\begin{aligned} \langle \tilde{b}_i \tilde{b}_i \rangle - \xi \partial_\xi \left\langle \frac{\tilde{b}_i \tilde{b}_i}{2} \right\rangle + \frac{1}{2\xi} \partial_\xi \left\langle \tilde{u}_3 \frac{\tilde{b}_i \tilde{b}_i}{2} \right\rangle + \frac{1}{2C\xi} \langle \tilde{u}_i \partial_\xi (\tilde{b}_1 \tilde{b}_i + \tilde{b}_2 \tilde{b}_i + C\tilde{b}_3 \tilde{u}_i) \rangle \\ + \frac{1}{2\sqrt{\rho_m} C \xi A g t} B_0 \langle \tilde{u}_i \partial_\xi \tilde{b}_i \rangle + \frac{1}{2\xi} \partial_\xi \langle \tilde{b}_3 \tilde{b}_i \tilde{u}_i \rangle = 0 \end{aligned} \quad (2.8)$$

Unlike the mass, momentum, and induction equations, the TKE and TME equations do not reduce to ODEs in ξ alone. This is due to the initial magnetic field term $\left(\frac{1}{2\sqrt{\rho_m} C \xi A g t} B_0 \langle \tilde{u}_i \partial_\xi \tilde{b}_i \rangle \right)$ which varies with ξ and t . That is, the solutions of TKE and TME equations are not functions of ξ alone, and hence not self-similar, unless the influence of initial magnetic field term is suppressed.

It is easy to see that the total turbulent energy (which is the sum of TKE and TME) is not effected by the imposed magnetic field. Adding equations 2.6 and 2.8, we get

$$2\langle \tilde{E} \rangle - \xi d_\xi \langle \tilde{E} \rangle + \frac{1}{2\xi} d_\xi \langle \tilde{u}_3 \tilde{E} \rangle + \frac{1}{2\xi} d_\xi \langle \tilde{u}_3 \tilde{p} \rangle + \frac{1}{2\xi} d_\xi \langle \tilde{b}_3 \tilde{b}_i \tilde{u}_i \rangle - \frac{1}{A} \langle \delta \tilde{\rho} \tilde{u}_i \delta_{i3} \rangle = 0, \quad (2.9)$$

where $\langle E \rangle = \langle \frac{\tilde{\rho} \tilde{u}_i \tilde{u}_i}{2} \rangle + \langle \frac{\tilde{b}_i \tilde{b}_i}{2} \rangle$. Equation 2.9 is an ODE in ξ and hence the total turbulent energy is a function of ξ .

To summarize the above analytical exercise, using the HD scaling for the ideal MHD equations, we found that some of the equations do not reduce to the self-similar form. Hence, from the proof of contradiction, we show that the MRTI does not have self-similar evolution of HD form. We showed that some of the imposed magnetic fields deviate the system from self-similar behaviour. The strength of the imposed magnetic field, however, varies as $1/t$. At $t \gg 1$, the non-linear terms dominate the dynamics leading the system towards self-similar evolution. As $t \rightarrow \infty$, the initial magnetic field term tends to zero. Thus at late time, when the system becomes highly non-linear, the MRTI evolution approaches towards self-similarity with scaling laws similar to the HD RTI.

2.2. Derivation of an expression for mixing layer height

In §2.1, we concluded that as the instability evolves the imposed magnetic field term decreases as $1/t$ and the MRTI converges towards self-similarity. But, how do the mixing layer height and other parameters grow in time in the self-similar regime? And how does the magnetic field strength change the growth constant of instability? Towards answering these questions, we will derive an analytical relation for the temporal variation of mixing layer height in the self-similar regime. The equation of mixing layer height gives us the temporal variation of velocity, and thus the temporal variations of TKE and TME.

From the conservation of energy, we know that the gravitational potential energy (GPE) released is the sum of turbulent kinetic energy (TKE), turbulent magnetic energy (TME),

and the energy dissipated up until that time, that is

$$-\underbrace{\int_V \rho g x_3 dV}_{\text{GPE released}} = \underbrace{\int_V \frac{1}{2} \rho u^2 dV}_{\text{TKE}} + \underbrace{\int_V \frac{1}{2} b^2 dV}_{\text{TME}} + \underbrace{\int_0^t \int_V D_E dV dt}_{\text{Total energy dissipated}}. \quad (2.10)$$

Under self-similarity, we assume that the total energy dissipated up to a given time is proportional to the total turbulent energy (sum of TKE and TME) i.e., $\int_0^t \int_V D_E dV dt \propto \int_V \left(\frac{1}{2} \rho u^2 + \frac{1}{2} b^2 \right) dV$. Let $\int_0^t \int_V D_E dV dt = C_{diss} \left(\int_V \frac{1}{2} \rho u^2 dV + \int_V \frac{1}{2} b^2 dV \right)$. Hence the above equation reduces to

$$-\underbrace{\int_V \delta \rho g x_3 dV}_{\text{Total GPE released}} = (1+C_{diss}) \left(\underbrace{\int_V \frac{1}{2} \rho u^2 dV}_{\text{TKE}} + \underbrace{\int_V \frac{1}{2} b^2 dV}_{\text{TME}} \right), \quad (2.11)$$

where $\delta \rho$ is the density fluctuation over initial density profile ($\delta \rho = \rho - \rho_0$) as defined in § 2.1.

From the self-similarity arguments, we expect that the TKE and TME are proportional to each other (i.e., $\text{TME} \propto \text{TKE}$). Let us consider, $\int_V \frac{1}{2} b^2 dV = C_{ep} \int_V \frac{1}{2} \rho u^2 dV$. Under this assumption, the above equation can be rewritten as

$$-\int_V \delta \rho g x_3 dV = (1+C_{diss})(1+C_{ep}) \left(\int_V \frac{1}{2} \rho u^2 dV \right). \quad (2.12)$$

The TKE constitutes energy from each component of velocity (i.e., $\int_V \frac{1}{2} \rho u^2 dV = \sum_{i=1}^3 \int_V \frac{1}{2} \rho u_i^2 dV$). The self-similarity implies that the TKE along the homogeneous directions (x_1, x_2) and the non-homogeneous direction (x_3) are proportional. That is, $\sum_{i=1}^2 \int_V \frac{1}{2} \rho u_i^2 dV \propto \int_V \frac{1}{2} \rho u_3^2 dV$. Let C_{aniso} be the proportionality constant, simplifying the above equation to

$$-\int_V \delta \rho g x_3 dV = (1+C_{diss})(1+C_{ep})(1+C_{aniso}) \left(\int_V \frac{1}{2} \rho u_3^2 dV \right). \quad (2.13)$$

Dividing the above equation with volume integrated density, we get

$$-g \frac{\int_V \delta \rho x_3 dV}{\int_V \rho dV} = (1+C_{diss})(1+C_{ep})(1+C_{aniso}) \frac{\int_V \frac{1}{2} \rho u_3^2 dV}{\int_V \rho dV}. \quad (2.14)$$

To derive the equation of mixing layer height (h) in terms of t , we need to write the quantities on the left and right hand sides of the above equation in terms of h or $\partial_t h$. In the region outside the mixing layer, $\delta \rho = 0$. Hence, the volumetric integral of $\delta \rho x_3$ is proportional to $V_m \bar{\rho} h$, where V_m is the volume of the mixing layer ($V_m = L_x L_y h$) and $\bar{\rho}$ is the volume averaged density. Let,

$$\frac{\int_V \delta \rho x_3 dV}{\int_V \rho dV} = C_{com} \frac{L_x L_y h \bar{\rho} h}{L_x L_y L_z \bar{\rho}} = C_{com} \frac{h^2}{L_z}. \quad (2.15)$$

We know that, growth rate of mixing layer is proportional to the vertical velocity of the mixing layer i.e., $\partial_t h \propto u_3$. In the region outside the mixing layer, $u_3 \approx 0$. Hence,

$\int_V \frac{1}{2} \rho u_3^2 dV \propto V_m \bar{\rho} (\partial_t h)^2$. Let

$$\frac{\int_V \frac{1}{2} \rho u_3^2 dV}{\int_V \rho dV} = \frac{1}{C_{gr}} \frac{L_x L_y h \bar{\rho} (\partial_t h)^2}{L_x L_y L_z \bar{\rho}} = \frac{1}{C_{gr}} \frac{h (\partial_t h)^2}{L_z}. \quad (2.16)$$

We chose the constant as $1/C_{gr}$ for the ease of calculating C_{gr} later when the RTI is modelled numerically. Implementing the above scaling, we get,

$$\frac{C_{com} g}{L_z} h^2 = \frac{(1+C_{diss})(1+C_{ep})(1+C_{aniso})}{C_{gr}} \frac{h (\partial_t h)^2}{L_z}, \quad (2.17)$$

Integrating the above equation with time using the separation of variable method, we get

$$h = \frac{C_{com} C_{gr}}{4A(1+C_{diss})(1+C_{ep})(1+C_{aniso})} A g t^2 + 2 \sqrt{\frac{C_{com} C_{gr}}{4A(1+C_{diss})(1+C_{ep})(1+C_{aniso})}} A g h_0 t + h_0, \quad (2.18)$$

where h_0 is the height of the mixing layer at $t=0$ assuming the mixing layer height had a quadratic variation from $t=0$. Equation 2.18 confirms that the mixing layer height of non-linear MRTI evolves quadratically in time even in the presence of magnetic field, similar to the HD RTI. Comparing the above equation with the equation of mixing layer for the HDRTI (equation 1.1), we deduce the growth rate constant for MRTI as

$$\alpha_{mhd} = \frac{C_{com} C_{gr}}{4A(1+C_{diss})(1+C_{ep})(1+C_{aniso})} \quad (2.19)$$

From the above equation, we see that the growth of instability is controlled by:

- i) the ratio of total energy dissipated to the total turbulent energy (C_{diss}),
- ii) the energy partition between TKE and TME (C_{ep}),
- iii) distribution of TKE among the homogeneous and the non-homogeneous components (C_{aniso}),
- iv) the scaling of the non-homogeneous component of TKE and GPE with their respective non-dimensional forms (C_{gr} , C_{com}).

It is important to keep in mind that the above coefficients (C_{diss} , C_{ep} , C_{aniso} , C_{gr} , C_{com}), and hence the growth constant (α_{mhd}), might vary with the magnetic field strength and the Atwood number. Analytical estimation of these constants at a given magnetic field strength, Atwood number is not possible, which necessitates the numerical modelling of MRTI to determine α_{mhd} . However, the advantage of having such a formula is the understanding it brings as to what parameters play an important role in the variation of α_{mhd} as the magnetic field strength and Atwood number changes. Further, the above formula also gives a hope towards obtaining the variation of non-linear growth constant with magnetic field strength and Atwood number. If a scaling relation of these coefficients with magnetic field or Atwood number can be established, it might be possible to construct a scaling relation for the non-linear growth constant with the magnetic field strength or Atwood number.

From equation 2.19, one might expect that in the Boussinesq limit ($A \rightarrow 0$) the α_{mhd} tends towards infinity. However, this is not the case. In the limit of small Atwood number the density varies linearly across the mixing layer height i.e., $\rho \propto x_3$ (Cook *et al.* 2004). Assuming a general linear form for density, one can obtain the density profile as $\rho = 2\rho_m(\frac{A}{h}x_3 + 1)$, where ρ_m is the arithmetic mean of the two densities ($\rho_m = \frac{\rho_h + \rho_l}{2}$). The term $\delta\rho x_3 dV$ can be written as

$$\int_V \delta\rho x_3 dV = L_x L_y \int_{-h/2}^{h/2} \left(\rho_0 - 2\rho_m \frac{A}{h} x_3 - 2\rho_m \right) x_3 dx_3 \quad (2.20)$$

$$\Rightarrow \int_V \delta \rho x_3 dV = L_x L_y \left(\int_{-h/2}^0 \rho_l x_3 dx_3 + \int_0^{h/2} \rho_h x_3 dx_3 - \int_{-h/2}^{h/2} 2\rho_m \frac{A}{h} x_3^2 \right) \quad (2.21)$$

$$\Rightarrow \int_V \delta \rho x_3 dV = L_x L_y \rho_m A h^2 / 12. \quad (2.22)$$

That is, at low Atwood number $C_{com} \propto A$ (since $\int_V \rho dV = L_x L_y L_z \bar{\rho}$). Thus α_{mhd} is restricted from blowing up through the quantity C_{com} .

Having determined the temporal variation of mixing layer height with time, we are in a position to determine the temporal variation of other quantities like momentum, turbulent magnetic field, TKE, and TME. We know that the (vertical) velocity of the mixing layer is of the order $\partial_t h$ (i.e., $O(t)$). The volume averaged momentum is expected to be of order $O(h)O(t)$ i.e., $O(t^3)$. Volume averaged TKE is of the order $h(\partial_t h)^2$ i.e., $O(t^2)O(t^2) = O(t^4)$. In terms of mixing layer height, $\int_V \text{TKE} dV$ is of the order h^2 . From self-similar scaling, $\int_V \text{TME} dV$ is expected to be of the same order, $O(t^4)$ or $O(h^2)$. The t^4 variation of TKE, TME agrees with the temporal scaling of TKE, TME reported in Stone & Gardiner (2007b).

To summarize, an equation for the mixing layer height in the self-similar regime is derived. The height of the mixing layer was found to grow quadratically in time, similar to the HD case. Comparing with the HD mixing layer height equation, a formula for the growth of instability was deduced. The formula shed light on various factors that could play a crucial role in the growth of instability. However, the growth rate at a particular field strength and its variation with field strength cannot be estimated without determining the coefficients, which necessitates the numerical modelling of MRTI. We will focus on the variation of the coefficients with magnetic field strength in this paper.

3. Numerical methodology

While a formula for α_{mhd} was obtained, the value of α_{mhd} for a given field strength remains unknown unless the values of the proportionality constants are obtained. Determining these constants demands numerical simulations of non-linear MRTI. Further, to evidence the validity of the assumptions made in the derivation of mixing layer height equation, and the conclusions of analytical study, we need to simulate the MRTI numerically. The current section details the methodology of the numerical simulation.

In the current study, MRTI was modelled by superimposing a high density fluid (ρ_h) over a low density fluid (ρ_l) in the presence of uniform, unidirectional magnetic (\mathbf{B}_0) and gravitational (\mathbf{g}) fields as shown in figure 3.1(a). The magnetic and gravitational fields are along the horizontal and vertical directions (parallel and perpendicular to the interface), respectively. The numerical modelling was performed using Dedalus (Burns *et al.* 2020), an open-source, parallelized computational framework to solve the partial differential equations using the spectral method. In the current study, we solve the non-ideal MHD governing equations mentioned below:

$$\partial_t \mathbf{u} + \nabla \tilde{p}' - \nu \nabla^2 \mathbf{u} = -(\mathbf{u} \cdot \nabla) \mathbf{u} - \frac{\tilde{p}'}{\rho} \nabla \rho - \frac{\delta \rho}{\rho} \mathbf{g} - \frac{1}{\rho} (\mathbf{B} \cdot \nabla) \mathbf{B}, \quad (3.1a)$$

$$\partial_t \mathbf{B} - \eta \nabla^2 \mathbf{B} - c_p^2 \nabla (\nabla \cdot \mathbf{B}) = (\mathbf{B} \cdot \nabla) \mathbf{u} - (\mathbf{u} \cdot \nabla) \mathbf{B}, \quad (3.1b)$$

$$\partial_t \rho - D \nabla^2 \rho = -(\mathbf{u} \cdot \nabla) \rho, \quad (3.1c)$$

$$\nabla \cdot \mathbf{u} = 0. \quad (3.1d)$$

Equation 3.1(a), (b), (c), and (d) are the Navier-Stokes equation, the induction equation, the mass continuity equation, and the incompressibility condition, respectively. \mathbf{u} , \mathbf{B} , ρ represent

the velocity, magnetic field, and density respectively. The modified pressure (\bar{p}') quantity, is the ratio of fluctuating pressure to the density ($\frac{P'}{\rho}$).

Dedalus demands the time derivative and linear terms of the equations on the left hand side of the equation. These linear terms form a sparse linear matrix, which is solved for the state variable using matrix inversion methods. This means the linear matrix should be invertible with non-zero divergence. A detailed methodology can be seen in Burns *et al.* (2020). Using ideal MHD equations (equation 2.1), the linear matrix becomes non-invertible since the determinant is zero. Hence, we solve the visco-resistive MHD equations. We consider two miscible fluids with equal and constant density diffusion coefficient (D) (Briard *et al.* 2024). The diffusion smooths sharp density gradients and aids mixing of fluids at grid scale. ν , η are the coefficients of fluid, and magnetic diffusion, respectively. The value of ν , η , D is set to 10^{-4} in the current study.

Despite introducing density, fluid, and magnetic diffusivities, it was found that a linear term for pressure is necessary to form an invertible linear matrix. Therefore, the non-linear pressure term $\frac{1}{\rho}\nabla P'$ is rewritten in terms of modified pressure as the sum of linear ($\nabla\bar{p}'$) and non-linear parts ($-\frac{\bar{p}'}{\rho}\nabla\rho$), where \bar{p}' is the the ratio of fluctuating pressure to density as defined in the previous paragraph. The fluctuating pressure includes hydrodynamic and magnetic pressures.

The solenoidal condition for magnetic field is ensured through divergence cleaning term ($c_p^2\nabla(\nabla\cdot\mathbf{B})$) (Dedner *et al.* 2002). In the current study, the value of c_p is set to 10 and the solenoid condition is satisfied to machine precision throughout the simulation for all the simulations.

Here, MRTI is studied in 2D and 3D with periodic boundary conditions in all directions. For 2D, a domain of length $L_x\times L_z=4\times 6$ units ($x : [0, L_x], z : [-\frac{L_z}{2}, \frac{L_z}{2}]$) with resolution of 2048×3072 is taken. For 3D, a domain of length $L_x\times L_y\times L_z=4\times 4\times 6$ units ($x : [0, L_x], y : [0, L_y], z : [-\frac{L_z}{2}, \frac{L_z}{2}]$) with resolution of $512\times 512\times 768$ is taken. The acceleration due to gravity is taken as 1. Since the purpose of the study is to understand the role of magnetic field on self-similarity, we present the results for a single Atwood number. We choose to study the problem at as large a density ratio as possible. Due to the choice of using a spectral solver, the maximum density ratio that can be used is limited. This is due to the ringing artifact caused at large sharp density jumps. While density diffusion aids smoothing the density jumps at grid scale, large density ratios lead to sharp density gradients resulting in ringing. For the chosen density diffusion coefficient, test simulations with increasing Atwood number showed ringing effect for $A>0.5$. Hence, Atwood number of 0.5 with $\rho_h=3$ and $\rho_l=1$ was chosen.

The initial density profile is given by equation 3.2 and shown in figure 3.1(a).

$$\rho = 1 - \frac{(\rho_h - \rho_l)}{2} \left[\tanh\left(\frac{z - 0.45L_z}{0.05}\right) + 1 \right] + \frac{(\rho_h - \rho_l)}{2} \left[\tanh\left(\frac{z}{0.05}\right) + 1 \right] \quad (3.2)$$

The above density profile is chosen to facilitate periodicity in the z -direction. The profile results in two interfaces, one at $z=0$ and the other at $z=0.90L_z$ as shown in figure 3.1(a). The transition between the two densities is made continuous using a hyperbolic tangent profile with a half width of $l=0.05$ (see equation 3.2). Thus, there are 25 or ≈ 7 grid points across the width of interface in 2D and 3D, respectively. As the MRTI evolves, the instability elongates the interface of two fluids over time. As the bubbles (and spikes) evolve the field lines get bundled around the bubbles (and spikes) resulting in thinner interface over time. While the density diffusion aids smoothing the density profile, it is important to ensure that the interface is initially resolved over an adequate number of grid points, so that there are a sufficient number of grid points at any point of time in the evolution. Hence, we chose half

width of 0.05 so that the interface remains adequately resolved in 3D. While the 2D MRTI case can have a smaller half width, we chose to use $l = 0.05$ to maintain consistency.

The upper interface is left unperturbed. Even if perturbed, it does not undergo RTI due to its stable configuration (high density fluid supporting the low density fluid). An advantage of the stable interface close to the top boundary is that it acts as a marker of boundary influence on flow structures. In the current system, as long as the top interface remains unaffected by the rising plumes, we can consider that the boundary influences are absent. The two interface density structure is also common among experimental (Suchandra & Ranjan 2023; Dalziel & Mouet 2021) and numerical (Briard *et al.* 2024, 2022) studies.

The lower interface ($z=0$) of the system is perturbed by a vertical velocity. In 2D, the perturbation is of the form

$$w = \sum_{i=1}^{128} a_i \sin\left(\frac{2\pi k_i x}{L_x} + \phi_i\right) e^{-(z^2/0.01)}. \quad (3.3)$$

The amplitude (a), wave mode (k), and phase (ϕ) of the perturbation are chosen between $[-0.0125, 0.0125]$, $[1, 128]$, and $[0, \pi]$, respectively. In 3D, the perturbation is of the form

$$w = \left(\sum_{i=0}^{64} a_i \sin\left(\frac{2\pi k_i x}{L_x} + \phi_i\right) \times \sum_{j=0}^{64} a_j \sin\left(\frac{2\pi k_j y}{L_y} + \phi_j\right) - \underbrace{(a_0 \sin \phi_0)}_{i=0} \times \underbrace{(a_0 \sin \phi_0)}_{j=0} \right) e^{-(z^2/0.01)}. \quad (3.4)$$

Here, a , k , and ϕ are chosen between $[-0.001, 0.001]$, $[1, 64]$, and $[0, \pi]$, respectively. We introduce wide range of wave modes in both 2D and 3D MRTI simulations as suggested by Ramaprabhu *et al.* (2005); Dalziel *et al.* (1999); Dimonte *et al.* (2004); Glimm *et al.* (2001). The perturbations decay in a Gaussian profile about the interface ($z=0$). The perturbed wave modes are in the homogeneous direction(s). The current simulation has only undular modes in 2D. In 3D, the system has undular ($i \neq 0, j = 0$), interchange ($i = 0, j \neq 0$), and a wide range of modes in between ($i \neq 0, j \neq 0$).

To test the self-similar evolution and determine the role of magnetic field strength on the non-linear growth of MRTI, we run MRTI simulations over a range of magnetic field strengths between $1\%B_c$ and $25\%B_c$ (for B_c , see equation 3.5). In 2D, eight cases of $B_0 = 0\%, 1\%, 2\%, 3\%, 5\%, 7\%, 10\%, 15\%$, and $25\%B_c$ were run. In 3D, seven cases of $B_0 = 0\%, 1\%, 2\%, 3\%, 5\%, 15\%, 25\%B_c$ were run. Here B_c refers to the critical magnetic field strength, the magnetic field strength at which the undular mode ($k \parallel B_0$ or $\theta = 0$) of the instability is completely suppressed (i.e., $\sigma=0$ cf. equation 1.2). From equation 1.2, it can be seen that for a given k , ρ_h , ρ_l , g , and $\theta (\neq \Pi/2)$, as the magnetic field strength is increased, the linear growth rate decreases. Substituting $\sigma = 0$ and $\theta = 0$ in equation 1.2, B_c can be obtained as

$$B_c = \sqrt{\frac{(\rho_h - \rho_l)g}{2k}}. \quad (3.5)$$

4. Results from numerical experiments

4.1. Role of magnetic field on the nature of mixing layer

In §1 we discussed how magnetic fields selectively suppress the perturbations in the linear regime. The wave modes smaller than the critical wave mode (k_c , see equation 1.3) result in instability. The evolution is shown for a weak 3D MRTI case ($B_0 = 1\%B_c$) is shown in figure 3.1(b, c, d) using density contours at various time instants. The distance from the

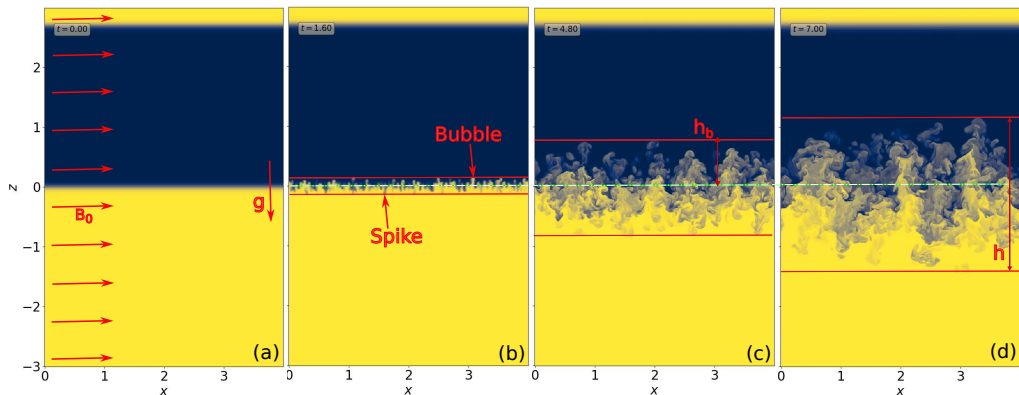


Figure 3.1: Figure showing the initial configuration (a), evolution (b, c, d) of magnetic Rayleigh-Taylor instability mixing layer through the density contours (2D slice at mid y-plane) at different time instants $t=1.6$, $t=4.80$, $t=7.0$ (from left to right). The snapshots correspond to $B_0 = 1\%B_c$ case. The red lines mark the boundaries of the mixing layer. The dashed white line is the center line $z=0$. The distance between the red lines is the height of mixing layer.

center (white dashed-dotted line) to the top and bottom boundaries of the mixing layer (red lines) are the height of bubbles (h_b), and spikes (h_s), respectively. The asymmetry of mixing layer (i.e., $h_b \neq h_s$) is a well known phenomenon, and the ratio of h_s/h_b is known to increase with density ratios (Hillier 2020). The evolution is similar for the 2D MRTI, except for the difference in the turbulence level in the mixing layer, explained below.

A fundamental difference between the 2D and 3D MRTI that influence the dynamics significantly is the nature of wave modes that evolve in the two cases. In the 2D simulations, we introduce unidirectional magnetic fields along x and the perturbed wave modes are along x . Hence, we only have undular modes. However, in the 3D case, the system is perturbed in the x and y directions, whereas the magnetic field is unidirectional along x . Hence, in 3D there exists a plane perpendicular to the magnetic field where the interchange modes can grow. Thus, we have a wide range of modes ($\theta \in [0, \Pi/2]$) growing in 3D MRTI making the mixing layer in 3D MRTI is more turbulent compared to 2D MRTI for a same magnetic field strength. For example, in figure 4.1, we present the density contours at the x -, and y -mid-planes for 2D and 3D MRTI at field strengths $B_0 = 5\%B_c$, and $25\%B_c$. From figure 4.1, the mixing layer is clearly more turbulent in the 3D case. This difference is particularly stark at $B_0 = 25\%B_c$, where the mixing layer is significantly turbulent in 3D MRTI, while the mixing layer is composed of laminar like plumes in 2D. However, this does not mean that the suppression of wave modes by the magnetic field is absent in 3D MRTI. While the mixing layer is turbulent at both 5% and $25\%B_c$ in 3D MRTI, we see the suppression of small scales (and hence turbulence) with increasing field strength (see figure 4.2). This can be quantitatively seen from figure 4.3 (left), where we plot the turbulent kinetic energy (TKE) scaled with released gravitational potential energy (GPE) for different magnetic field strengths.

So why is the amount of TKE reducing with increasing B_0 ? Assuming the flux frozen condition (a reasonable assumption when magnetic reconnection (Priest & Forbes 2000) is not occurring given low magnetic diffusivity, $\eta = 10^{-4}$), the fluid lines are strongly coupled to magnetic field lines and the evolution of instability demands the deformation of both fluid lines and magnetic field lines. As the imposed magnetic field strength is increased, the field lines have a greater magnetic tension and destabilizing the field lines demands a

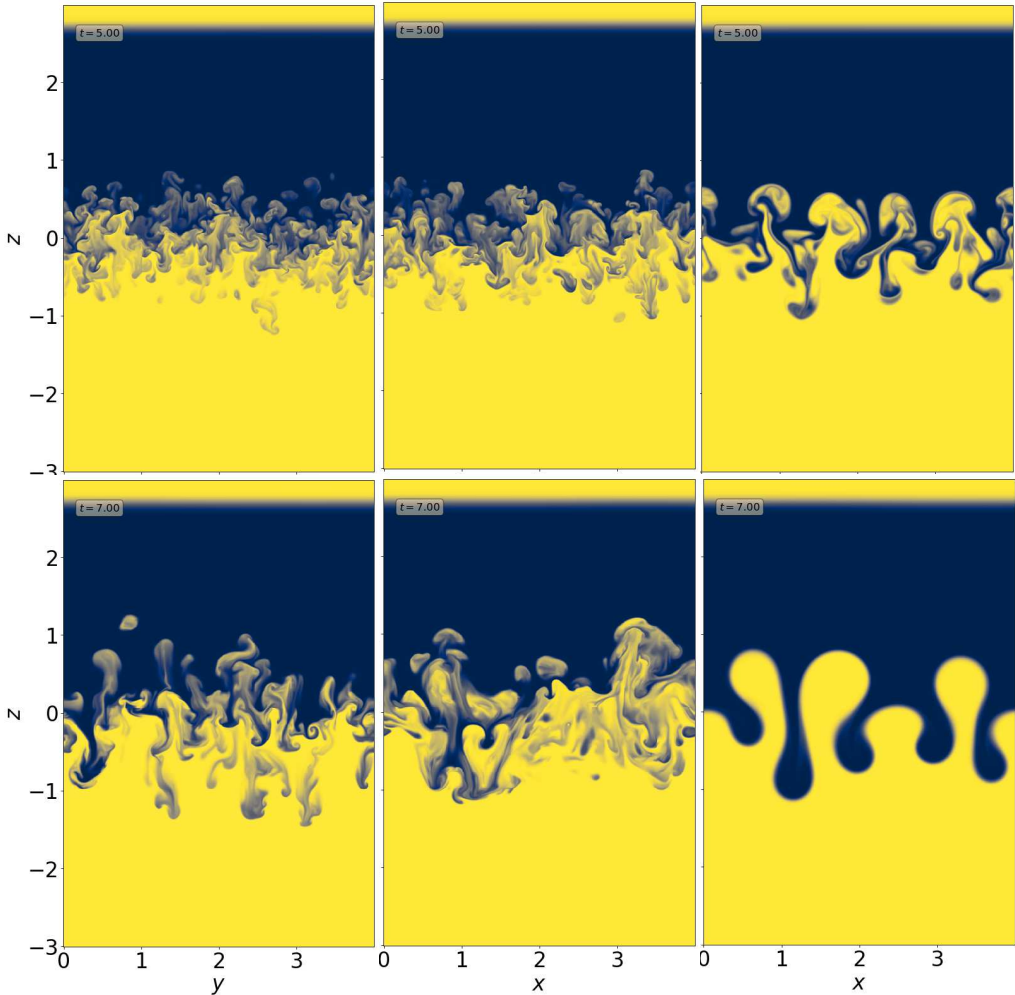


Figure 4.1: Qualitative comparison of 3D MRTI (left and middle) and 2D MRTI (right) mixing layers through density contours at time $t = 5$ for the magnetic field strength $B_0 = 5\%B_c$ (top row), and at time $t = 7$ for $B_0 = 25\%B_c$ (bottom row).

greater proportion of GPE. This means the amount of energy converted to TME increases with increasing field strength, which can be seen from figure 4.3(right). As a consequence of increasing TME, TKE reduces. One might notice that the sum of TKE and TME (scaled by GPE) is not exactly equal to 1. This is due to the energy dissipation due to the non-ideal terms.

The suppression of turbulence and mixing for the strong magnetic fields were reported in the previous studies (Stone & Gardiner 2007b; Carlyle & Hillier 2017). It was proposed that the reduced mixing could be due to suppression of small scale shear by the magnetic field. Here, we present a clearer picture of magnetic fields suppress the mixing through the density contours and magnetic field lines. Due to strong coupling between the fluid lines and the magnetic field lines, as the instability evolves the magnetic field lines wrap around the plumes as shown in figure 4.4. The flux frozen condition meant that the material is restricted to a field line (i.e., material transport across the field lines is not allowed) preventing the mixing of fluids of different densities. From the conservation of magnetic

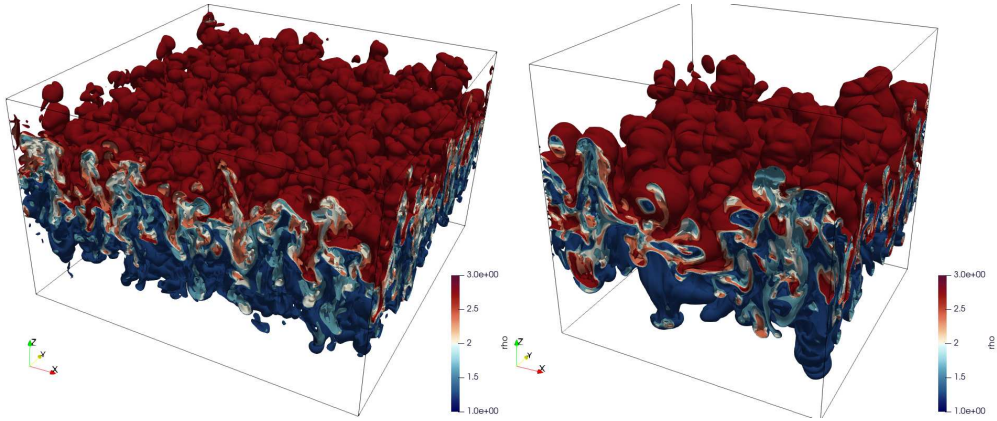


Figure 4.2: Qualitative comparison of 3D MRI mixing layers through iso-surfaces of density at time $t = 5$ for the magnetic field strength $B_0 = 5\%B_c$, and at time $t = 7$ for $B_0 = 25\%B_c$.

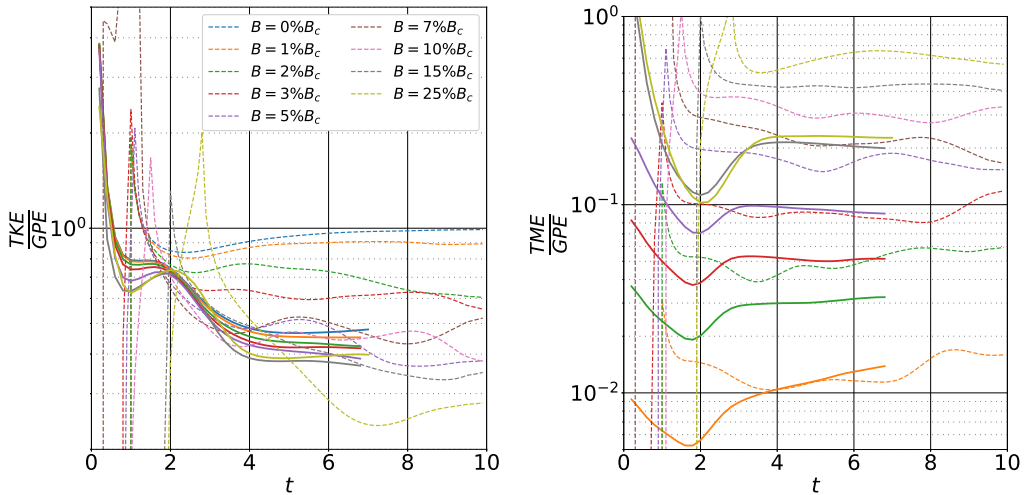


Figure 4.3: Temporal variation of: (left) turbulent kinetic energy; (right) turbulent magnetic energy over time for different magnetic field strengths. The turbulent kinetic energy and turbulent magnetic energy are scaled with the released gravitational potential energy. The legend in the right figure is same as the left one. The 2D and 3D cases are shown as dashed and solid lines respectively.

flux, the stretching of magnetic field lines at the interface of two fluids lead to bundling of field lines around the bubbles and reduction in the width of the interface (see figure 4.4). This creates sharp interfaces where the fluids shear during rising of bubbles or falling of spikes. Since the magnetic field is oriented parallel to the shearing plane, other sources of mixing like the Kelvin-Helmholtz instability that develop due to shearing are suppressed efficiently by the magnetic field. The suppression of KHI due to magnetic fields is a well known phenomenon (Hughes & Tobias 2001). The other source of intermediate density fluid in the strong magnetic field case is the density diffusion.

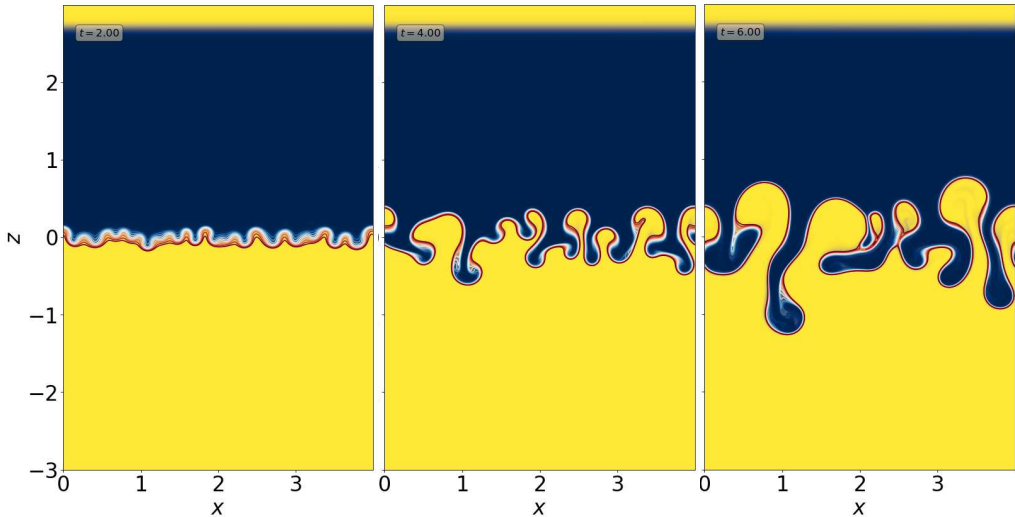


Figure 4.4: Snapshots of density contour and magnetic field lines showing the evolution of 2D MRTI for $B_0=15\%B_c$.

4.2. Role of magnetic field on self-similarity

4.2.1. Numerical evidence of the temporal scaling

Having discussed the suppression of turbulence and mixing in the MRTI mixing layer due to the magnetic field, we will look into the temporal variation of initial magnetic field term ($B_0\langle u_i\partial_1 b_i \rangle$), mixing layer height, turbulent kinetic energy (TKE) and turbulent magnetic energy (TME) in the self-similar regime for different magnetic field strengths from the numerical simulations.

To understand the scaling of initial magnetic term relative to the other terms of the TKE equation (2.5), we plot the temporal ratio $\int_V B_0 u_i \partial_1 b_i dV / \int_V \delta \rho g_i u_i \delta_{i3} dV$ for different magnetic field strengths in figure 4.5. From equation 2.6, we expect the ratio of these two terms to vary as $1/t$ in the self-similar regime. From the figure 4.5 we see that in 3D the imposed magnetic field term decays as $1/t$ with time relative to the gravity term. However, the approximate constant value of the ratio in 2D case implies a fixed scaling between the two quantities, and the self-similar behaviour of the imposed magnetic field term. Nevertheless, in both 2D and 3D the system converges towards the self-similar behaviour even if the $1/t$ scaling is only present in 3D models.

From §2.2, we expect that the height of mixing layer h has a quadratic variation with time, and the volume averaged TKE and TME to have t^4 variation, in the self-similar region. To confirm this numerically, we plotted the temporal variation of h/t^2 , TKE/t^4 , and TME/t^4 for different magnetic field strengths (see figure 4.6). The time between the \blacklozenge is considered as the self-similar regime. The methodology of determining the self-similar time frame is explained later. To verify the temporal scaling of h , TKE and TME, the quantities h/t^2 , TKE/t^4 , and TME/t^4 were sampled in the self-similar regime and their standard deviation is calculated. The standard deviation of the quantities were found to be well within the 1σ limit (34%) of the mean value for most cases, and can hence be considered to be approximately constant. In the context of scaling, it is also worth mentioning that the volume averaged TKE and TME have the h^2 scaling, as claimed in the analytical study (§2.2). The plot is not shown here for brevity.

In the current study, the height of the mixing layer is calculated based on the mixing

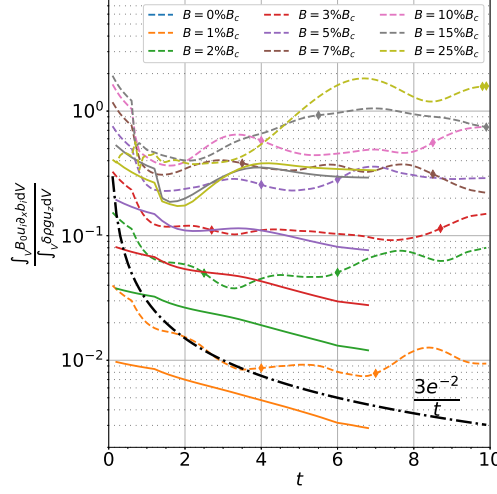


Figure 4.5: Temporal variation of the initial magnetic field term ($\int_V B_0 u_i \partial_1 b_i dV$) relative to the gravity term ($\int_V \delta \rho g_i u_i \delta_{i3} dV$) of TKE equation 2.5 for different magnetic field strengths for both 2D (dashed lines) and 3D (solid lines) cases. The black dash-dotted line shows the curve $0.03/t$.

parameter $\Theta = 4 \frac{\langle \rho \rangle - \rho_l}{\rho_h - \rho_l} \frac{\rho_h - \langle \rho \rangle}{\rho_h - \rho_l}$ (Stone & Gardiner 2007b). $\langle \star \rangle$ refers to averaging along the statistical homogeneous directions. Outside the mixing layer where the density is either ρ_h or ρ_l , $\Theta = 0$. The value of Θ lies between $(0, 1]$ in the mixing layer. $\Theta = 1$ is the well mixed condition, when $\langle \rho \rangle = \frac{\rho_h + \rho_l}{2}$. Since the density considered to calculate Θ is spatially averaged along the statistically homogeneous directions, Θ is only a function of z . The boundaries of mixing layer were defined taking a threshold value of Θ . We choose the threshold for Θ as $10\% \Theta_{max}$. The core of the mixing layer, where the two fluids mix have high Θ , and as we move towards the boundaries of the mixing layer, the value of Θ decreases. The point along z at which Θ drops below 0.1 is considered as the boundary of the mixing layer. The boundaries of the mixing layer above and below the center line ($z = 0$) is considered as the height of bubble (h_b) and height of spike (h_s), respectively. The height of the mixing layer is the sum of the magnitudes of h_b and h_s . It is worth noting that there are several other ways of choosing the boundaries of mixing layer, discussed in Baltzer & Livescu (2020). However, we use the current method in-line with the other MRTI studies (Jun *et al.* 1995; Stone & Gardiner 2007b,a; Carlyle & Hillier 2017).

4.2.2. Estimation of non-linear growth constant

Having confirmed the convergence of the system towards self-similarity and the approximate quadratic variation of the mixing layer height (cf. figure 4.6), we will now determine the non-linear growth constant using numerical curve fitting techniques. Figure 4.7 shows the temporal variation of mixing layer height for different magnetic field strengths. From equation 2.18, the height of mixing layer follows $h = \alpha_{mhd} Ag t^2 + 2\sqrt{\alpha_{mhd} Ag h_0} t + h_0$ in the self-similar regime. First, we define a quadratic function $\hat{y} = a\hat{x}^2 + b\hat{x} + c$, where the input parameters of \hat{x} and \hat{y} are t and h , respectively. The input data for the above formulation is sampled between the self-similarity time frame. The obtained coefficients are scaled by Ag to determine α_{mhd} numerically. To verify the accuracy of the α_{mhd} obtained from the curve fitting method, we also calculated the α_{mhd} from $(\partial_t h)^2 = 4\alpha_{mhd} Ag h$ formulation (Cabot & Cook 2006). The value α_{mhd} obtained are consistent from both the cases. Figure 4.7 (right) shows the value of

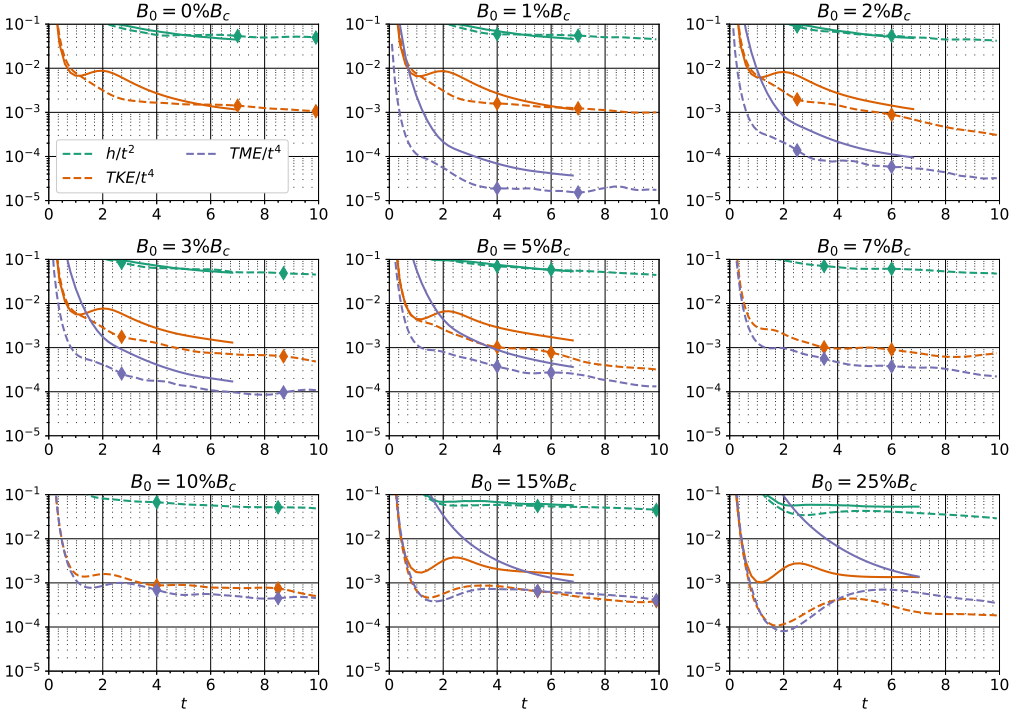


Figure 4.6: Temporal variation of mixing layer height (h), turbulent magnetic energy (TME), and turbulent kinetic energy (TKE) for different field strengths. h , TKE, and TME are scaled by t^2 , t^4 , and t^4 respectively. The 2D and 3D cases are shown as dashed and solid lines respectively.

α_{mhd} determined from the curve fitting technique for both 2D MRTI (\diamond with dotted line) and 3D MRTI (\diamond with dashed line). It can be seen that the α_{mhd} has a different trend in 2D and 3D. While the non-linear growth constant decreases with increasing field strength in 2D, in 3D the non-linear growth constant increases with increasing field strength. The trend of α_{mhd} obtained for the 3D MRTI case is in agreement with the previous study by Stone & Gardiner (2007b). It is worth mentioning that similar to the studies so-far, at the moment, we are not in a position to explain why α_{mhd} increases (3D case) or decreases (2D case) with the imposed magnetic field strength (B_0). However, later in the article, based on the derived analytical formula of α_{mhd} (equation 2.19) we will look into the different physical processes and will explain the reason for this variation of α_{mhd} with B_0 .

It must be noted that while the mixing layer does have a quadratic behaviour, the growth of mixing layer is predominantly dominated by the linear growth than the quadratic growth, particularly in the 3D MRTI with weak magnetic fields. This behaviour was also observed in the experimental studies at Atwood number 0.5 (Suchandra & Ranjan 2023). From our numerical study, the coefficient of the linear term ($2\sqrt{\alpha_{mhd}Ag h_0}$) is approximately 7 times the coefficient of quadratic term ($\alpha_{mhd}Ag$) for the weaker 3D MRTI case ($B_0 \leq 5\%B_c$). For the stronger 3D MRTI case ($B_0 \geq 15\%B_c$) and all 2D MRTI cases the coefficient of the linear term is typically 3 times the coefficient of quadratic term. This stronger linear growth is also evident from the profile of temporal variation of mixing layer shown in figure 4.7 (left).

The self-similarity time frame in the current study is determined from $\int_V \rho u_z u_z dV$

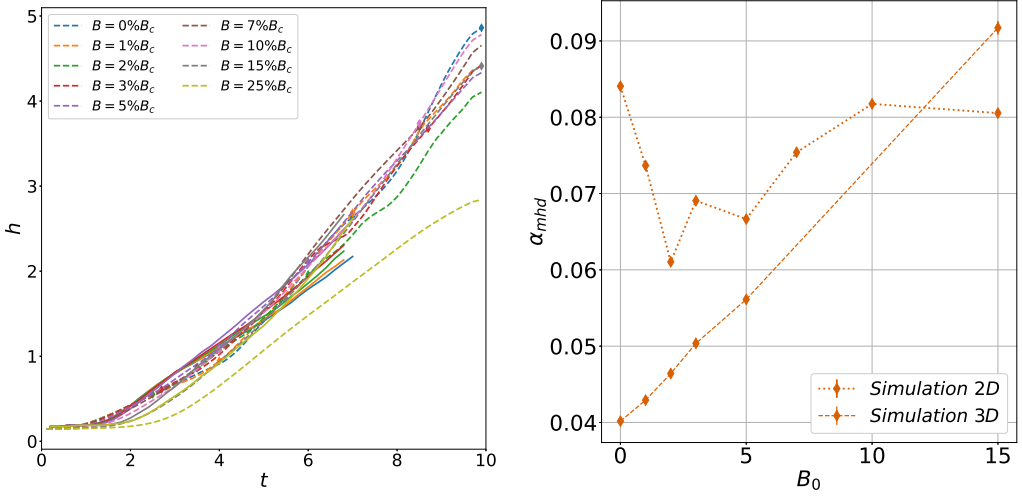


Figure 4.7: (left) Temporal variation of mixing layer height (h) for different magnetic field strengths. The \diamond symbol represent the proposed self-similar time frame. The 2D and 3D cases are shown as dashed and solid lines respectively. (right) Variation of α_{mhd} with magnetic field strength for 2D and 3D cases.

(Rogers & Moser 1992; Baltzer & Livescu 2020) and later verified based on other quantities like, energy dissipation (Rogers & Moser 1994; Baltzer & Livescu 2020) and the ratio of TME to TKE. In § 2 we argued that the TKE and TME are proportional to each other in the self-similar regime. This is based on the reasoning that the turbulent magnetic field vary proportionally to the turbulence in the system. Hence, the time frame during which the vertical kinetic energy, the energy dissipation, and the ratio of TME to TKE is approximately constant is considered as the time frame of self-similarity. We consider that a statistical quantity to be approximately constant if the variation is within 1σ limit (34%) of the mean value. In figure 4.8, we plot the temporal variation of vertical kinetic energy (non-dimensionalised by the released gravitational potential energy) for each magnetic field strength. The time frames of self-similarity are marked in \diamond . We note that the $\int_V \rho u_z u_z dV$ is approximately constant with a standard deviation less than 12% of the mean value for all magnetic field strengths. We will show that the quantities, TME to TME ratio, and energy dissipation are approximately constant in the self-similar regime in §4.2.3.

4.2.3. Verification of self-similarity assumptions

Having verified the quadratic growth of mixing layer and the self-similarity, we will now further verify the assumptions made in §2.2 to derive the equation of mixing layer height (equation 2.18). This would further reinforce the argument that MRTI has a self-similar behaviour, proposed in §2.1. We begin with the assumption, in the self-similar regime, the total energy dissipated up until time t is proportional to the total turbulent energy in the system. With the introduction of the magnetic field, the total energy dissipated (D_E) in MRTI is the sum of energy dissipated due to TKE (D_{TKE}) and TME (D_{TME}). For a visco-resistive MHD system, the energy dissipated is calculated as

$$D_E = \underbrace{\int_t \int_V \nu \rho (\partial_j u_i)^2 dV dt + \int_t \int_V (\nu + D) (\partial_j \rho) \left(\partial_j \frac{u_i u_i}{2} \right) dV dt}_{\text{TKE dissipation } (D_{TKE})} + \underbrace{\int_t \int_V \eta (\partial_j b_i)^2 dV dt}_{\text{TME dissipation } (D_{TME})}. \quad (4.1)$$

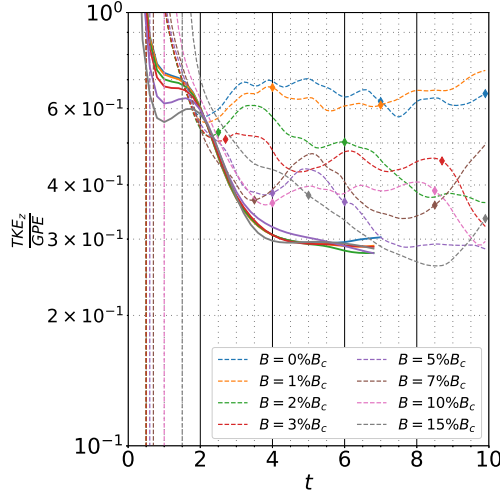


Figure 4.8: Temporal variation of vertical kinetic energy ($\int_V \rho u_z u_z dV$) non-dimensionalized by released gravitational potential energy ($\int_V \delta \rho g z dV$) for different magnetic field strengths. The 2D and 3D cases are shown by dashed and solid lines respectively.

The terms $\int_t \int_V \nu \rho (\partial_j u_i)^2 dV dt$ and $\int_t \int_V \eta (\partial_j b_i)^2 dV dt$ are always positive. However, the term $\int_t \int_V (\nu + D) (\partial_j \rho) (\partial_j \frac{u_i u_i}{2}) dV dt$ can be negative or positive.

Figure 4.9(left) shows the temporal variation of energy dissipation non-dimensionalized by the total turbulent energy (C_{diss} , cf. $\int_0^t \int_V D_E dV dt = C_{diss} \left(\int_V \frac{1}{2} \rho u^2 dV + \int_V \frac{1}{2} b^2 dV \right)$). For any given magnetic field strength, C_{diss} is approximately constant over the time frame marked by \blacklozenge , with standard deviation less than 15%. This shows that the system is self-similar in the considered time frame. The self-similar duration obtained from the energy dissipation also agrees well with the self-similarity time frame obtained from the vertical kinetic energy (figure 4.8). The approximate constant ratio also demonstrates the self-similar scaling between the energy dissipation and total turbulent energy.

From figure 4.9(left) it is evident that the energy dissipation varies with the magnetic field strength. To quantify the energy dissipation coefficient we sample the parameter C_{diss} in the marked self-similar region and obtain the mean and standard deviation of C_{diss} . Figure 4.9 (right) shows the mean (\blacktriangleright) and standard deviation (represented as error bar) values of C_{diss} for different B_0 values of the 2D MRTI (connected with dashed line) and 3D MRTI (connected with solid line). For both 2D and 3D cases, the dissipation is maximum for $B_0 = 5\% B_c$ case, where the energy dissipated is $\approx 33\%$ and $\approx 50\%$ of the released GPE. Thus, even a marginal addition of magnetic field seem to increase the dissipation significantly. Beyond the $5\% B_c$ energy dissipation decreases with increasing field strength in both 2D and 3D MRTI. A potential reason for the smaller dissipation at strong magnetic field strength could be due to the reduced vortices and current sheets which are the hotspots of the energy dissipation. Figure 4.10 shows the contours of vorticity (top panel) and current (bottom panel) for two cases of 2D MRTI, $B_0 = 3\% B_c$ (left panel) and $B_0 = 15\% B_c$ (right panel), at the same time instant $t = 8$. It is clear that energy dissipation is predominantly due to current sheets for both the magnetic field strengths. Comparing the two field strengths, one can also see that while the energy dissipation due to TKE only marginally reduced between 3% and $15\% B_c$, energy dissipation due to TME has significantly reduced when magnetic field is increased from 3% to $15\% B_c$.

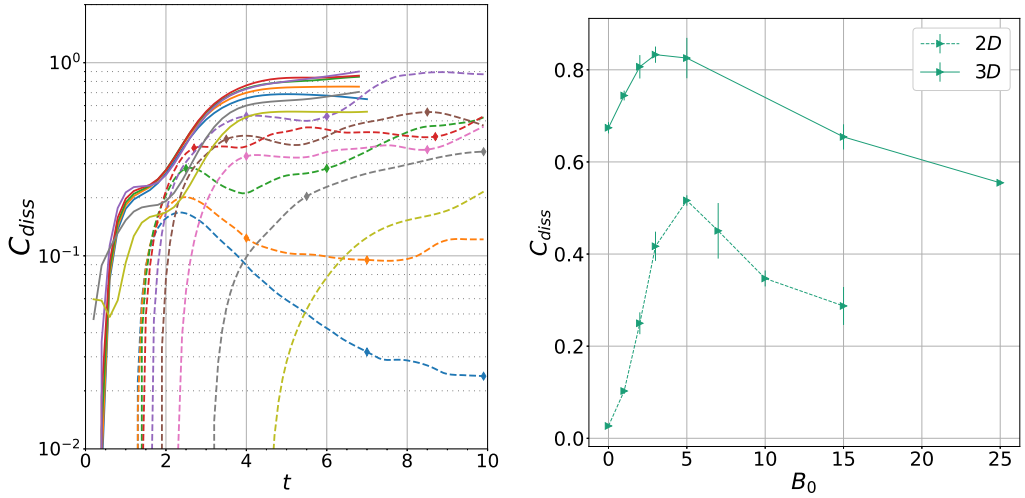


Figure 4.9: (left) Ratio of dissipation energy to total turbulent energy over time for different magnetic field strengths. The inset figure shows the same but in log scale in y -axis to demonstrate the constants of proportionality. (right) Variation of C_{diss} with magnetic field strength. The 2D and 3D cases are shown as dashed and solid lines respectively. The legend is same as figure 4.8 for both the left and right figures.

The next assumption is the scaling of TKE and TME in the self-similar region. This is again confirmed by plotting their ratio over time as shown in figure 4.11 (left). For each magnetic field case the ratio is approximately constant (the standard deviation is less than 12% of the mean value) in the considered self-similar time frame. This further reinforces that accuracy of the considered self-similar time frame. The approximate constant ratio also evidences that the two quantities are proportional to each other at all the magnetic field strengths. Their ratio is referred to as C_{ep} from now on (cf. $\int_V \frac{1}{2} b^2 dV = C_{ep} \int_V \frac{1}{2} \rho u^2 dV$). Both the 2D and 3D studies show that the C_{ep} varies significantly with the imposed field strength. From figure 4.3, with increasing magnetic field strength, TME increases and TKE decreases. Hence their ratio (C_{ep}) increases with magnetic field strength. The mean (\bullet) and standard deviation (error bar) of C_{ep} in the self-similar time period was calculated as described for C_{diss} case. C_{ep} increases with B_0 for 2D and 3D MRTI (see figure 4.11 (right)). However, while the C_{ep} is quantitatively similar for the 2D and 3D MRTI in weak field regime ($B_0 \leq 5\% B_c$), in the strong field regime C_{ep} is significantly smaller for 3D compared to 2D. This is due to the significant suppression of perturbed wave modes in the 2D MRTI compared to the 3D MRTI.

The next assumption is the scaling of the homogeneous and non-homogeneous kinetic energies. As before, we plot the ratio of TKE along the homogeneous directions ($\frac{1}{2}\rho u_x^2 + \frac{1}{2}\rho u_y^2$) to the TKE along non-homogeneous direction ($\frac{1}{2}\rho u_z^2$) against time as shown in figure 4.12(left). For the 2D case, since $u_y = 0$, $C_{aniso} = \frac{1}{2}\rho u_x^2 / \frac{1}{2}\rho u_z^2$. The same time used in the C_{diss} is considered here for the self-similarity. The mean (\blacksquare) and standard deviation (error bar) of C_{aniso} obtained from the self-similar duration is shown in figure 4.12 (right). C_{aniso} was found to decrease with increasing magnetic field strength for both 2D and 3D MRTI. That is, the proportion of TKE in the homogeneous direction is higher in weak field case, which reduces with increasing field strength. A potential reason for this is the reduction of vortical structures with increasing field strength (see figures 4.1 (top panel vs bottom panel), 4.10 (left panel)). The strong vorticity in the weak magnetic

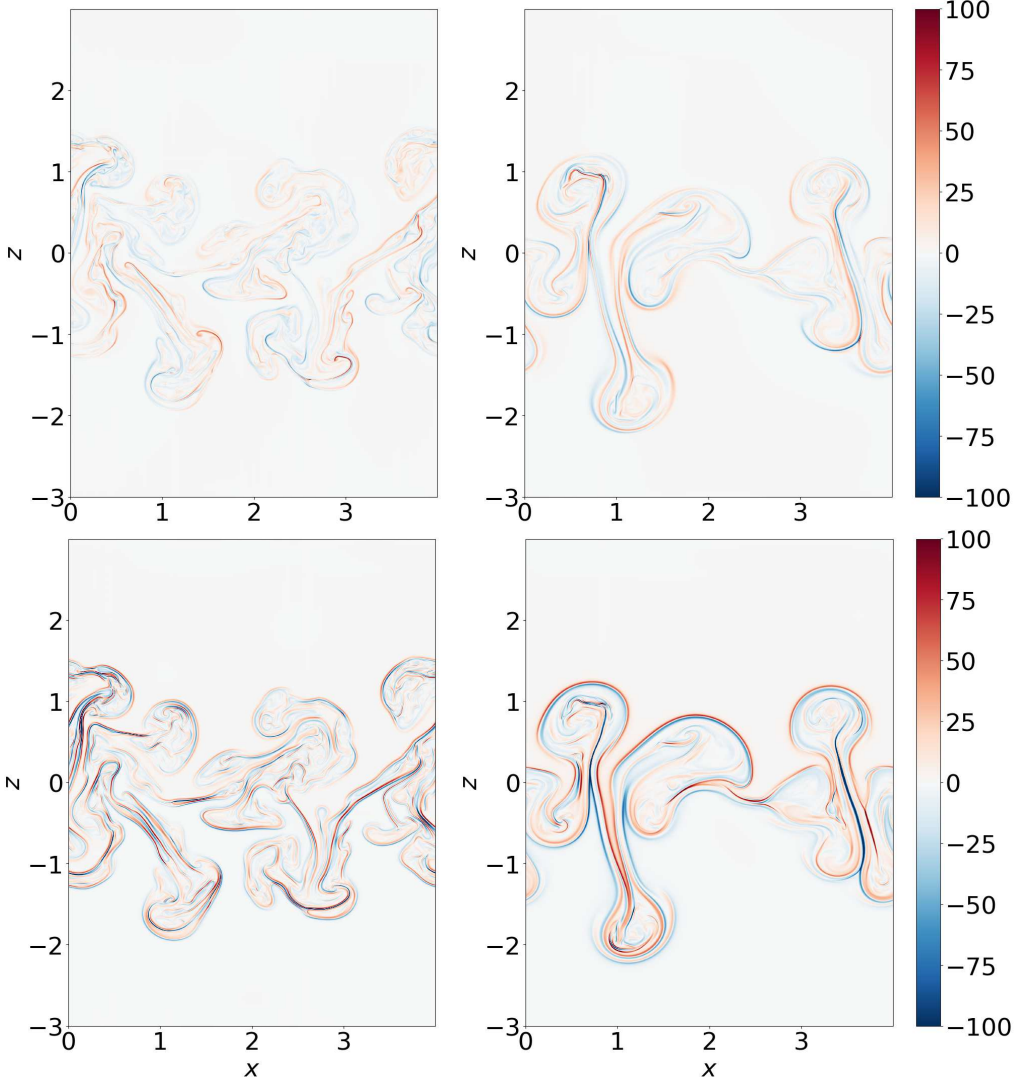


Figure 4.10: Instantaneous contours of vorticity (top panel, (a), (b)) and current (bottom panel, (c) and (d)) for two 2D MRTI cases, $B_0 = 3\%B_c$ (left panel, (a) and (c)) and $B_0 = 15\%B_c$ (right panel, (b) and (d)).

field case increases the redistribution of energy from non-homogeneous to homogeneous directions. Due to the reduction of the vortical structures at large magnetic fields, the energy is mostly in the non-homogeneous direction increasing anisotropy (i.e., decreasing C_{aniso}). The increase in anisotropy with increasing magnetic field strength is previously observed in the MHD turbulence (Shebalin *et al.* 1983). For the case of 2D MRTI, since the limit of energy distribution is equi-partition ($u_x = u_z$), C_{aniso} is always less than or equal to 1. In the case of 3D, under the assumption perfect energy distribution across all directions, $\frac{1}{2}\rho u_x^2 = \frac{1}{2}\rho u_y^2 = \frac{1}{2}\rho u_z^2$ which limits the C_{aniso} to a maximum value of 0.667.

Now that the self-similar assumptions made in the derivation of mixing layer height were verified, we consider that the system has converged to self-similarity in the considered time frame. Next, towards deriving an equation of the mixing layer height, we wrote the vertical

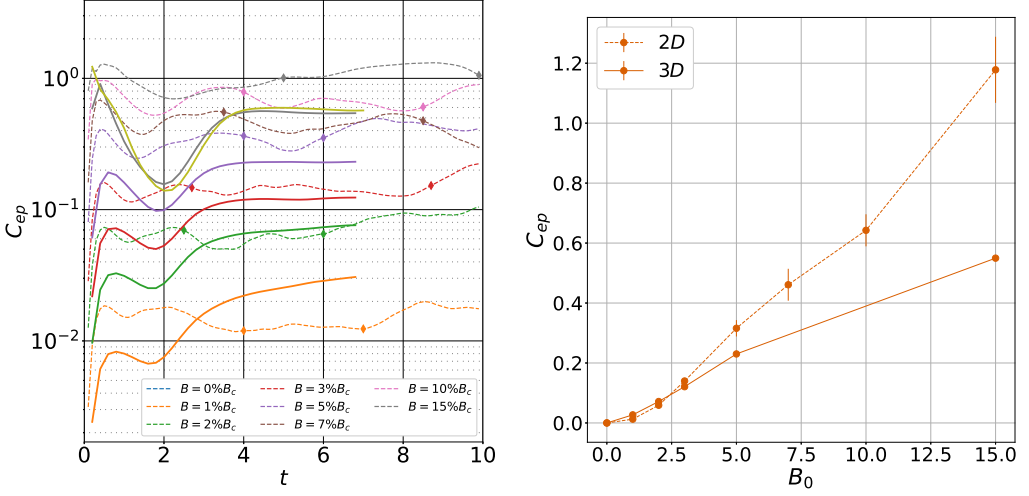


Figure 4.11: (left) Temporal variation of turbulent magnetic energy (TME) and turbulent kinetic energy (TKE) ratio. (right) Variation of C_{ep} with magnetic field strength. The 2D and 3D cases are shown as dashed and solid lines respectively. The legend for the right figure is same as the left one.

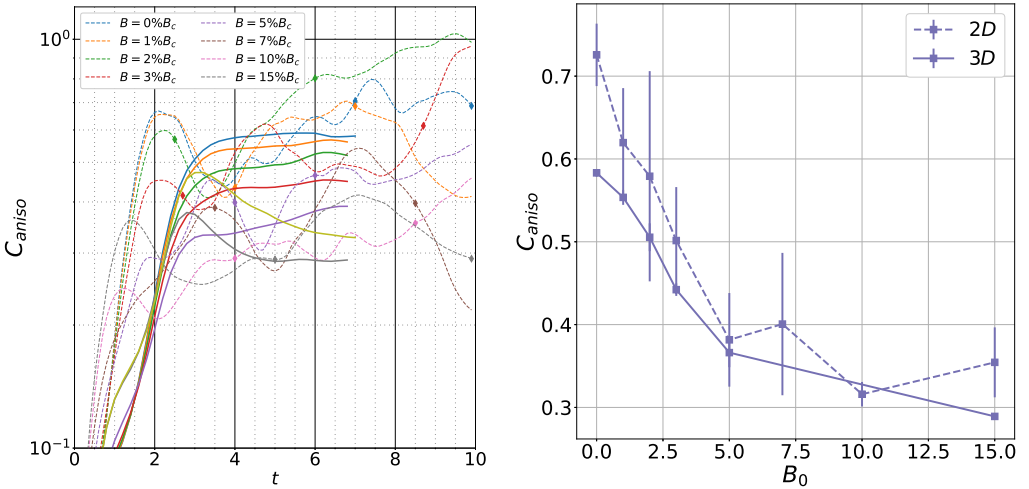


Figure 4.12: (left) Ratio of turbulent kinetic energy due to x - and y -components of velocity to the z -component of velocity over time for different magnetic field strengths; (right) The variation of anisotropy (C_{aniso}) with magnetic field strength. The 2D and 3D cases are shown as dashed and solid lines respectively.

kinetic energy ($\int_V \rho u_z^2 dV$) in terms of mixing layer height as $\frac{1}{C_{gr}} \frac{1}{L_z} \bar{\rho} h (\partial_t h)^2$. Physically, this tells the correlation between the vertical kinetic energy and the growth rate of mixing layer height. In figure 4.13(left), the ratio of these two quantities was plotted with time for both 2D and 3D MRTI. The time gradient result in high fluctuations in 2D and 3D, and hence the data is smoothed using a rolling mean with a window of 0.3 time units, shown as dashed lines. The raw data is not shown here for legibility. The ratio is C_{gr} .

The statistical mean and standard deviation of the C_{gr} is shown in figure 4.13 (right). In general, C_{gr} seem to increase with increasing magnetic field strength. From figure 4.12

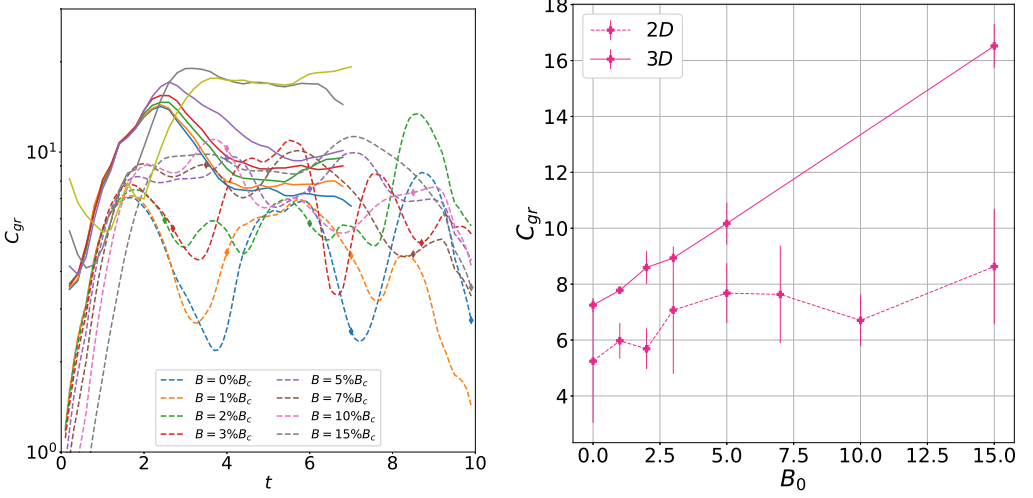


Figure 4.13: (left) Ratio of growth rate of mixing layer to the z -component of velocity (C_{gr} , cf. equation 2.16) over time for different magnetic field strengths; (right) The variation of (C_{gr}) with magnetic field strength. The 2D and 3D cases are shown as dashed and solid lines respectively.

(right), we see that as we increase the field strength, the proportional of TKE along the non-homogeneous component increases. The absence of small scale vortical structures that redistribute energy into other components of velocity in the strong magnetic field case (evident from figure 4.1) makes the vertical velocity is primarily invested towards the growth of mixing layer height in the vertical direction. Hence we expect to see an increasing value of the proportionality constant between the vertical kinetic energy and the growth rate of mixing layer height with increasing field strength.

Lastly, the released GPE ($\int_V \delta \rho g z dV$) was written in terms of mixing layer height as $C_{com} \frac{1}{L_z} \bar{\rho} h^2$. To calculate C_{com} , we plot the ratio of $L_z \int_V \delta \rho g z dV$ to $\bar{\rho} h^2$. Figure 4.14(left) shows the temporal variation of the quantity for 2D and 3D MRTI. The mean and standard deviation of C_{com} in the self-similar time frame is plotted in figure 4.14(right). C_{com} does not vary significantly with the field strength for 2D (≈ 0.06) and 3D (≈ 0.04). The approximate constant value of C_{com} obtained in the 3D MRTI case is in contradiction to the results of Carlyle & Hillier (2017) where they found that the center of mass of the mixing layer change with the field strength, but for a large density contrast.

4.2.4. Growth rate of mixing layer

Having confirmed the self-similar nature of the system and determined the scaling coefficients (C_{diss} , C_{ep} , C_{aniso} , C_{gr} , C_{com}), the value of α_{mhd} can be calculated from the analytical formula 2.19. To calculate the value of α_{mhd} from the derived analytical formula 2.19, we calculate the mean value of α_{mhd} as below:

$$\bar{\alpha}_{mhd} = \frac{\overline{C_{com} C_{gr}}}{4A(1+\overline{C_{diss}})(1+\overline{C_{ep}})(1+\overline{C_{aniso}})}. \quad (4.2)$$

The standard deviation of α_{mhd} in each case is calculated using

$$\sigma(\alpha_{mhd}) = \bar{\alpha}_{mhd} \left(\frac{\sigma(C_{diss})}{\overline{C_{diss}}} + \frac{\sigma(C_{ep})}{\overline{C_{ep}}} + \frac{\sigma(C_{aniso})}{\overline{C_{aniso}}} + \frac{\sigma(C_{gr})}{\overline{C_{gr}}} + \frac{\sigma(C_{com})}{\overline{C_{com}}} \right), \quad (4.3)$$

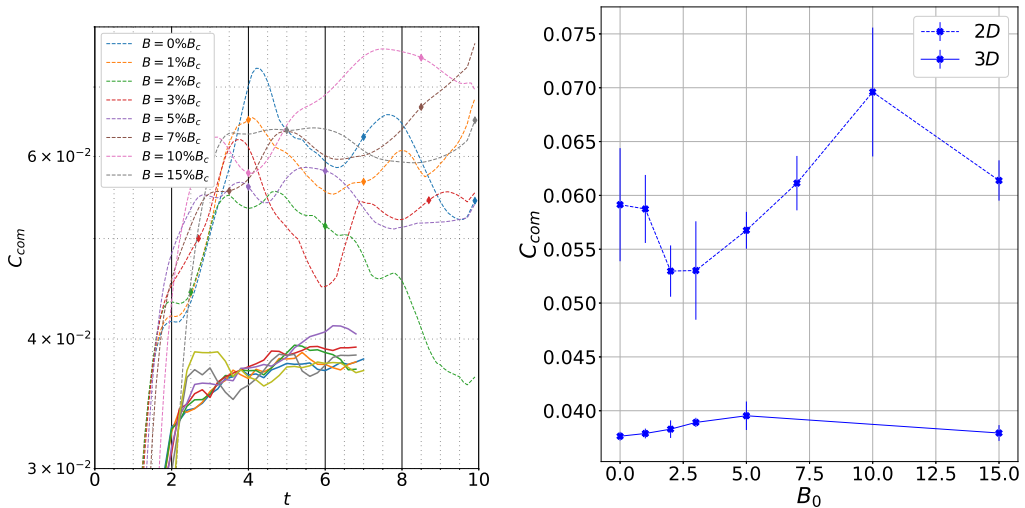


Figure 4.14: (left) Temporal variation of center of mass of the mixing layer (C_{com} , cf. equation 2.15) for different magnetic field strengths; (right) The variation of (C_{com}) with magnetic field strength. The 2D and 3D cases are shown as dashed and solid lines respectively.

where $\sigma(\phi)$, $\bar{\phi}$ represents the standard deviation and mean of ϕ . The variation of α_{mhd} with the imposed magnetic field was plotted in figure 4.15 for both 2D MRTI (blue ● connected via dotted line) and 3D MRTI (blue ● connected via dashed line). For both the cases, the circles show the value of α_{mhd} based on the mean quantities and the error bar shows the standard deviation of α_{mhd} . The α_{mhd} values have a different trend in 2D and 3D. In the case of 2D, except for the anomalous $1\%B_c$ case, we find a general trend of approximately constant α_{mhd} ($< \alpha_{B=0}$) between 2% and $10\%B_c$ where the mixing layer is turbulent. Beyond this regime when the magnetic field is strong enough to suppress the turbulence significantly we see decreasing α_{mhd} with increasing magnetic field strength. In the case of 3D, we see an increase in the growth rate with increasing magnetic field strength.

For the sake of comparison, in figure 4.15, we included the α_{mhd} calculated from numerical simulations. We see that the trend of α_{mhd} obtained from analytical formula are, in general, in agreement with the α_{mhd} from numerical simulations for both 2D and 3D MRTI. The exception case in 2D is the $1\%B_c$ case, where the value of α_{mhd} increased marginally. This is due to sharp increase in anisotropy (decreasing C_{aniso}) and growth rate (C_{gr}), while the energy dissipation and energy partition increase only marginally. In the case of 3D MRTI, the α_{mhd} obtained from analytical and numerical methods are significantly different in the weak field limit ($B_0 < 5\%B_c$). A potential reason for this could be the quadratic fitting being forced in the magnetic field regime where the growth is significantly dominated by the linear growth (see §4.2.2).

4.3. Scaling laws of constants

While the values of scaling coefficients (C_{diss} , C_{ep} , C_{aniso} , C_{gr} , C_{com}) at different magnetic field strengths were calculated, as of now they remain independent and estimating the growth rate at an intermediate magnetic field strength requires simulating MRTI numerically with the required field strength. However, this can be avoided if we can obtain a scaling law for the variation of these coefficients with the magnetic field strength. Towards this, we first develop

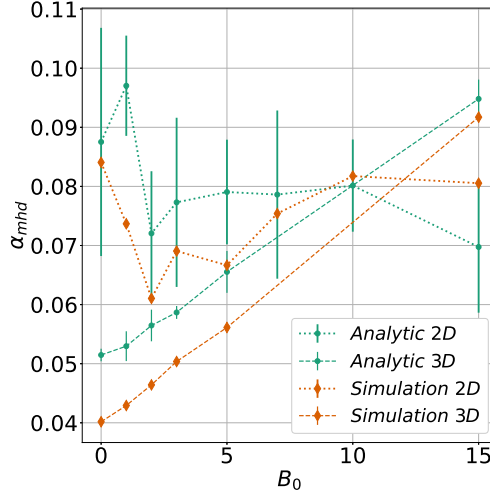


Figure 4.15: Comparison of α_{mhd} obtained from the numerical simulation against the α_{mhd} from analytical formula. The figure shows the α_{mhd} from the two formulations (quadratic, shown by orange squares and linear, shown by green diamonds)

the scaling laws building from the previous studies, and verify if the current results match the proposed scaling laws.

Towards this direction, we would first look at the energy dissipation. As mentioned before, in MRTI, the energy dissipation happens because of turbulent kinetic energy and turbulent magnetic energy, which can be assumed as ηj^2 and $\nu \rho \omega^2$, where j is the current, ω is the vorticity. The quantities ηj^2 and $\nu \rho \omega^2$ can be assumed to scale as $\eta b_{rms}^2 / l_j^2$ and $\nu \rho u_{rms}^2 / l_\omega^2$, respectively. Here l_j and l_ω are the length scales of characteristic current sheets and characteristic vorticity, b_{rms} and u_{rms} correspond to RMS values of turbulent magnetic field and turbulent velocity. Hence the total energy dissipation is proportional to the sum of $\eta b_{rms}^2 / l_j^2$ and $\nu \rho u_{rms}^2 / l_\omega^2$ i.e.,

$$D_E \propto \left(\eta \int_t \int_V \frac{b_{rms}^2}{l_j^2} dV dt + \nu \int_t \int_V \frac{\rho u_{rms}^2}{l_\omega^2} dV dt \right). \quad (4.4)$$

$$\Rightarrow D_E \propto \left(\eta \int_t \int_V \frac{C_{ep} \rho u_{rms}^2}{l_j^2} dV dt + \nu \int_t \int_V \frac{\rho u_{rms}^2}{l_\omega^2} dV dt \right), \quad (4.5)$$

since C_{ep} is defined as the energy partition between TME and TKE, $C_{ep} = \left(\frac{\int_V b_{rms}^2 dV}{\int_V \rho u_{rms}^2 dV} \right)$.

The above equation can be rewritten as

$$\Rightarrow D_E \propto \left(\frac{l_\omega^2}{l_j^2} \frac{1}{Pr_m} C_{ep} + 1 \right) \int_t \int_V \nu \frac{\rho u_{rms}^2}{l_j^2} dV dt, \quad (4.6)$$

where Pr_m is the magnetic Prandtl number (ν/η).

From the above equation, to obtain the scaling relation for the energy dissipation, we need to obtain the scaling relation for the energy partition between the turbulent kinetic and magnetic energies (TKE, TME, respectively) first. The energy gained by the magnetic field depend on the range of the scales suppressed by the magnetic field. Thus, the energy

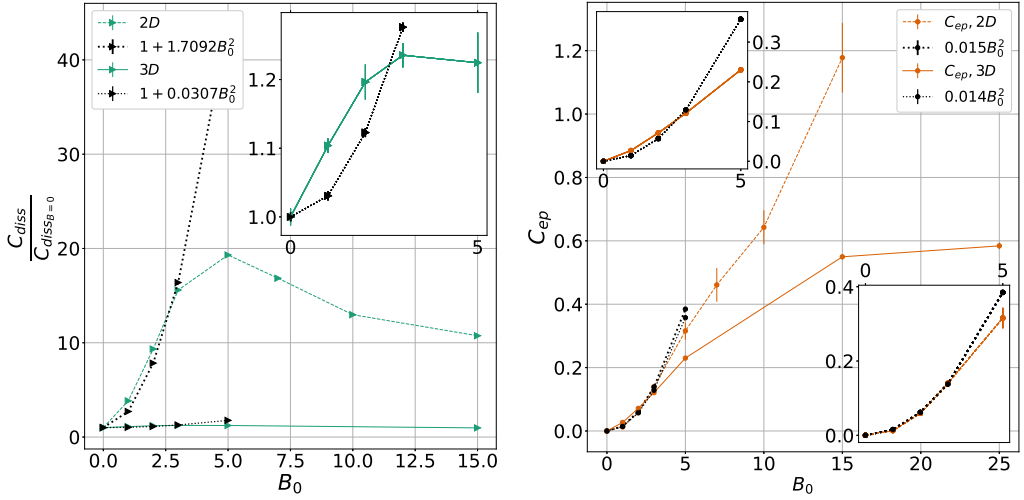


Figure 4.16: Variation of C_{diss} (left) and C_{ep} (right) with increasing magnetic field strength. Figure also shows the comparison of the variation of C_{diss} and C_{ep} with B_0 based on the scaling laws reported in equations 4.9 and 4.7.

partition between the TME and TKE are adequately obtained from the linear analysis. In the linear regime, Hillier (2016) showed that the energy partition between the turbulent magnetic energy and turbulent kinetic energy varies quadratically with imposed magnetic field strength i.e.,

$$\frac{\int_V b_{rms}^2 dV}{\int_V \rho u_{rms}^2 dV} \propto B_0^2. \quad (4.7)$$

Thus, C_{ep} is expected to be proportional to B_0^2 .

Based on the equation 4.7, we can obtain the scaling law for energy dissipation from the equation 4.6 as shown below,

$$D_E \propto \left(\frac{l_\omega^2}{l_j^2} \frac{1}{Pr_m} a B_0^2 + 1 \right) \int_t \int_V v \frac{\rho u_{rms}^2}{l_j^2} dV dt. \quad (4.8)$$

where a is a constant of proportionality. Thus, we expect the energy dissipation to scale quadratically with B_0 . In the hydrodynamic limit ($B_0 = 0$), energy dissipation reduces to dissipation due to TKE as expected. Dividing both sides of above with total turbulent energy (TKE + TME), we can show that

$$C_{diss} \propto \left(\frac{l_\omega^2}{l_j^2} \frac{1}{Pr_m} a B_0^2 + 1 \right) C_{diss_{B=0}}. \quad (4.9)$$

The above theories and scaling laws are applicable only to the turbulent mixing layers ($B_0 < 5\% B_c$, see figure 4.16). In the case of stronger magnetic fields, where the mixing layer is less turbulent or characterized by laminar like plumes, the above arguments does not apply and we might have to seek help from other models like the buoyancy-drag model (Schilling 2020; Youngs & Thornber 2020) to explain the variation of these quantities with magnetic field.

In our current study for both the 2D and 3D cases we found that the anisotropy is increasing (i.e., C_{aniso} is decreasing) with increasing field strength (see figure 4.13). A

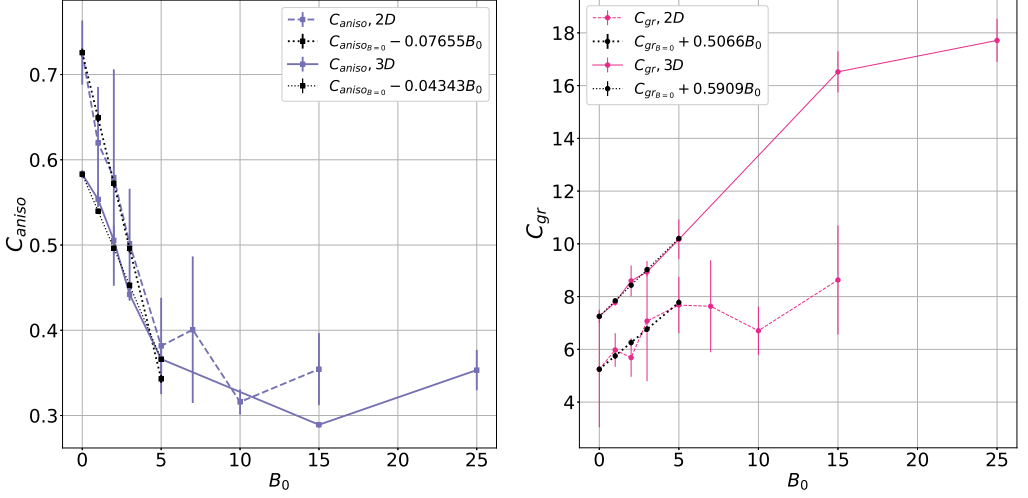


Figure 4.17: Variation of C_{aniso} (left) and C_{gr} (right) with increasing magnetic field strength. Figure also shows the comparison of the variation of C_{aniso} and C_{gr} with B_0 based on linear fitting.

potential reason for this is the decreasing vorticity in the system (see figure 4.10) with increasing magnetic field strength. The consequence of decreasing vorticity is decrease in the redistribution of turbulent kinetic energy into the homogeneous directions from the non-homogeneous direction leading to increasing anisotropy. The study by Shebalin *et al.* (1983) on homogeneous turbulent system reported similar results of increasing anisotropy with increasing magnetic field strength. However, to our knowledge, no study so far provides a scaling relation for the variation of anisotropy with the magnetic field strength. Our current 2D and 3D numerical simulations show that anisotropy increases (i.e., C_{aniso} decreases) linearly with the magnetic field strength upto $B_0 \leq 5\%B_c$. Similar linear variation of anisotropy with magnetic field strength were found by Shebalin *et al.* (1983) in the weak field limit. A comparison of the variation of C_{aniso} with the magnetic field strength along with the linear curve fitting is shown in figure 4.17 (left). Our 2D and 3D numerical studies show that in the stronger magnetic field regime, the anisotropy saturates to a fixed value. This is also in agreement with the results of Shebalin *et al.* (1983).

Both the 2D and 3D numerical simulations show that temporal growth rate of mixing layer height per unit non-homogeneous TKE is increasing linearly with magnetic field strength. The variation of C_{gr} with magnetic field strength along with the linear curve fitting is shown in figure 4.17 (right).

Having obtained the variation of various physical processes and their scaling laws with the magnetic field strength (cf. figures 4.9, 4.11, 4.12, 4.13, 4.14) we are now in a position to answer the question, why the α_{mhd} increase (decrease) with increasing magnetic field strength in 3D (2D). In the case of 2D MRTI, the energy dissipation and energy partition play a significant role. The energy partition C_{ep} which is 0 in the hydrodynamic case start to increase with the magnetic field strength. Similarly, the total energy dissipated is only due to TKE in the hydrodynamic case. With the introduction of magnetic fields, energy dissipated is due to both TKE and TME, increasing the total energy dissipation. The increase in energy dissipation and energy partition reduce the non-linear growth constant. As we go to regimes of strong magnetic fields, the influence of energy partition significantly dominates over other physical processes, and hence C_{ep} controls the non-linear growth constant. The

other quantities C_{com} and $\frac{C_{gr}}{(1+C_{aniso})}$ is approximately constant. In 3D MRTI, similar to the 2D case, the energy dissipation and the energy partition increase with field strength which should decrease the α_{mhd} . However, the quantity $\frac{C_{gr}}{(1+C_{aniso})}$, which is approximately constant in 2D, increases when it comes to 3D increasing the non-linear growth constant.

5. Discussion

Towards validating the appropriateness of the HDRTI scaling to the MRTI, and understanding the role of magnetic field on the self-similar evolution, we performed an analytical self-similar analysis using the hydrodynamic scaling in §2. The analytical study confirmed that, when sufficiently evolved, MRTI converges towards self-similar evolution with HD scaling. By sufficiently evolved, we refer to the state where the influence of imposed initial magnetic field is dominated by the non-linear terms. The study gave an insight into the role of imposed magnetic field in deviating the evolution from self-similarity. The equation of mixing layer height showed that, in the self-similar regime, the MRTI mixing layer has a quadratic growth, similar to the HD case. Integrating the equation of mixing layer height derived for the MRTI into the generalized Rayleigh-Taylor instability problem, it can be said that the Rayleigh-Taylor instability evolves quadratically in time in both the hydrodynamic and magnetic field cases. Considering the HDRTI is an extreme case of the MRTI with $B_0=0$, it is meaningful that the mixing layer height of MRTI and HDRTI grow quadratically.

While the profile of temporal variation remains same, the magnetic field demonstrates its effect through the growth constant (α_{mhd}). The formula of α_{mhd} derived (equation 2.19) gives an insight into the physical processes that could influence the non-linear growth of instability. The applicability of the formula to both hydrodynamic and magnetic field cases, makes it a good tool to understand what factors cause the change in α_{mhd} and how α_{mhd} varies as we transit from the HD limit to various magnetic field strength cases. To further elaborate on this, we found that the important factors that could influence the non-linear growth constant are the energy dissipation, the energy partition between the turbulent magnetic energy (TME) and the turbulent kinetic energy (TKE). In the HDRTI, the available energy is predominantly converted to TKE, and TME is zero, that is $C_{ep} = 0$. Also the energy dissipation is solely due to the TKE dissipation and hence, the energy dissipation is minimal in the HD case. With the introduction of magnetic fields, the available energy is partitioned between TKE and TME resulting in non-zero positive i.e., $C_{ep} > 0$. Also the total energy dissipation C_{diss} , which is the sum of energy dissipated due to TKE and TME, increases. This could lead to decrease in α_{mhd} . The same trend of decrease α_{mhd} with increasing magnetic field strength was observed from the analytical and numerical results.

An interesting aspect found in the current study is the significant increase in energy dissipation with marginal addition of magnetic field (discussed in §4.2.3). While a deeper investigation into this is needed, a potential reason for the drastic increase in the dissipation could be the disruption of vortices due to magnetic reconnection (Weiss & Adams 1966; Mak *et al.* 2017). The study by Mak *et al.* (2017) showed that marginal addition of magnetic fields lead to disruption of vortices, resulting in enhanced dissipation. However, increase in magnetic field strength beyond a certain limit could result in torsional oscillations of vortices without vortex disruption and leading to lesser energy dissipation with increasing magnetic field strength. It is possible that the vortex disruption is most significant at $B_0 = 5\%B_c$ and is mitigated by increased magnetic tension beyond this field strength.

6. Conclusion

Following the quadratic growth of mixing layer height, the studies so-far assumed that the non-linear MRTI has a self-similar evolution with scaling similar to HD RTI. However, no rigorous analytical or numerical study was performed to prove the self-similar quadratic growth of mixing layer. Towards this, the current study explored the validity of self-similar HDRTI scaling for the MRTI evolution. A case of uniform, unidirectional magnetic field is considered. Analytical self-similar analysis using the ideal MHD equations showed that the imposed magnetic field deviates the system from self-similar behaviour in the early stages. However, the influence of initial magnetic field decays overtime as $1/t$, and the non-linear turbulent quantities dominate the dynamics which drive the system towards self-similarity. Thus, the MRTI converges to hydrodynamic like self-similarity, when sufficiently evolved.

A formula for the non-linear growth constant in the self-similar regime was derived. The formula highlighted various parameters that could play a crucial role in determining the non-linear growth of the MRTI. For 2D MRTI with undular modes, the growth rate was found to be predominantly influenced by energy dissipation and energy partition in the weak magnetic field case where the mixing layer is turbulent. For the case of strong fields, where the mixing layer is characterised by laminar like plumes, energy partition is the influential parameter. In the 3D MRTI, the coefficient mixing layer growth per unit vertical kinetic energy is the key parameter.

The quadratic growth of mixing layer height and the formula of the α_{mhd} were tested numerically. The study found a good agreement between the α_{mhd} values obtained from analytical formula, and numerical simulations. Scaling relations of various parameters with magnetic field strength were obtained. The study, thus, presents a comprehensive understanding on the role of magnetic field on the evolution of instability, analytically and numerically. Further a detailed interpretation on the variation of non-linear growth constant with magnetic field is presented.

Supplementary data.

Acknowledgements. For the purpose of open access, the author has applied a ‘Creative Commons Attribution (CC BY) licence to any Author Accepted Manuscript version arising from this submission.

Funding. The first author is supported by the Engineering and Physical Sciences Research Council (EPSRC) Grant No. EP/W523859/1. AH is supported by STFC Research Grant No. ST/R000891/1 and ST/V000659/1. The computational time for this work was obtained from the University of Exeter High-Performance Computing (HPC) facility. This work used the DiRAC Memory Intensive service (Cosma7) at Durham University, managed by the Institute for Computational Cosmology on behalf of the STFC DiRAC HPC Facility (www.dirac.ac.uk). The DiRAC service at Durham was funded by BEIS, UKRI and STFC capital funding, Durham University and STFC operations grants. DiRAC is part of the UKRI Digital Research Infrastructure.

Declaration of interests. The authors report no conflict of interest.

Data availability statement. The data that support the findings of this study are available from the corresponding author upon reasonable request.

Author ORCIDs. M. T. Kalluri, <https://orcid.org/0000-0002-5441-9224>; A. Hillier, <https://orcid.org/0000-0002-0851-5362>

Author contributions. M.T.K.: data curation, formal analysis, investigation, methodology, software, validation, visualization, writing —original draft, review and editing; A.H.: conceptualization, funding acquisition, project administration, resources, supervision, writing—review and editing.

- BALTZER, JON R. & LIVESCU, DANIEL 2020 Variable-density effects in incompressible non-buoyant shear-driven turbulent mixing layers. *Journal of Fluid Mechanics* **900**, A16.
- BRIARD, ANTOINE, GRÉA, BENOÎT-JOSEPH & NGUYEN, FLORIAN 2022 Growth rate of the turbulent magnetic rayleigh-taylor instability. *Phys. Rev. E* **106**, 065201.
- BRIARD, A., GRÉA, B.-J. & NGUYEN, F. 2024 Turbulent mixing in the vertical magnetic rayleigh–taylor instability. *Journal of Fluid Mechanics* **979**, A8.
- BURNS, KEATON J., VASIL, GEOFFREY M., OISHI, JEFFREY S., LECOANET, DANIEL & BROWN, BENJAMIN P. 2020 Dedalus: A flexible framework for numerical simulations with spectral methods. *Phys. Rev. Research* **2**, 023068.
- CABOT, WILLIAM H. & COOK, ANDREW W. 2006 Reynolds number effects on Rayleigh–Taylor instability with possible implications for type Ia supernovae. *Nature Physics* **2** (8), 562–568.
- CARLYLE, JACK & HILLIER, ANDREW 2017 The non-linear growth of the magnetic rayleigh-taylor instability. *A&A* **605**, A101.
- CHANDRASEKHAR, SUBRAHMANYAN 1961 *Hydrodynamic and hydromagnetic stability*. Oxford University Press.
- COOK, ANDREW W., CABOT, WILLIAM & MILLER, PAUL L. 2004 The mixing transition in rayleigh–taylor instability. *Journal of Fluid Mechanics* **511**, 333–362.
- DALZIEL, S. B., LINDEN, P. F. & YOUNGS, D. L. 1999 Self-similarity and internal structure of turbulence induced by rayleigh–taylor instability. *Journal of Fluid Mechanics* **399**, 1–48.
- DALZIEL, STUART B. & MOUET, VALENTIN 2021 Rayleigh–taylor instability between unequally stratified layers. *Physica D: Nonlinear Phenomena* **423**, 132907.
- DEDNER, A., KEMM, F., KRÖNER, D., MUNZ, C.-D., SCHNITZER, T. & WESENBERG, M. 2002 Hyperbolic divergence cleaning for the mhd equations. *Journal of Computational Physics* **175** (2), 645–673.
- DIMONTE, GUY, YOUNGS, D. L., DIMITS, A., WEBER, S., MARINAK, M., WUNSCH, S., GARASI, C., ROBINSON, A., ANDREWS, M. J., RAMAPRABHU, P., CALDER, A. C., FRYXELL, B., BIELLO, J., DURSI, L., MACNEICE, P., OLSON, K., RICKER, P., ROSNER, R., TIMMES, F., TUFO, H., YOUNG, Y.-N. & ZINGALE, M. 2004 A comparative study of the turbulent rayleigh–taylor instability using high-resolution three-dimensional numerical simulations: The alpha-group collaboration. *Physics of Fluids* **16** (5), 1668–1693, arXiv: <https://doi.org/10.1063/1.1688328>.
- FERMI, E & VON NEUMANN, J 1953 Taylor instability of incompressible liquids. part 1. taylor instability of an incompressible liquid. part 2. taylor instability at the boundary of two incompressible liquids. *Tech. Rep.*. Los Alamos National Laboratory (LANL), Los Alamos, NM (United States).
- FRASCHETTI, F., TEYSSIER, R., BALLE, J. & DECOURCHELLE, A. 2010 Simulation of the growth of the 3d rayleigh-taylor instability in supernova remnants using an expanding reference frame. *A&A* **515**, A104.
- GLIMM, J., GROVE, J.W., LI, X.L., OH, W. & SHARP, D.H. 2001 A critical analysis of rayleigh–taylor growth rates. *Journal of Computational Physics* **169** (2), 652–677.
- HESTER, J. JEFF, STONE, JAMES M., SCOWEN, PAUL A., JUN, BYUNG-IL, GALLAGHER, JOHN S., III, NORMAN, MICHAEL L., BALLESTER, GILDA E., BURROWS, CHRISTOPHER J., CASERTANO, STEFANO, CLARKE, JOHN T., CRISP, DAVID, GRIFFITHS, RICHARD E., HOESSEL, JOHN G., HOLTZMAN, JON A., KRIST, JOHN, MOULD, JEREMY R., SANKRIT, RAVI, STAPELFELDT, KARL R., TRAUGER, JOHN T., WATSON, ALAN & WESTPHAL, JAMES A. 1996 WFPC2 Studies of the Crab Nebula. III. Magnetic Rayleigh–Taylor Instabilities and the Origin of the Filaments. *The Astrophysical Journal* **456**, 225.
- HILLIER, ANDREW 2018 The magnetic Rayleigh–Taylor instability in solar prominences. *Reviews of Modern Plasma Physics* **2** (1), 1.
- HILLIER, A. 2020 Self-similar solutions of asymmetric rayleigh-taylor mixing. *Physics of Fluids* **32** (1), 015103, arXiv: <https://doi.org/10.1063/1.5130893>.
- HILLIER, ANDREW S. 2016 On the nature of the magnetic Rayleigh–Taylor instability in astrophysical plasma: the case of uniform magnetic field strength. *Monthly Notices of the Royal Astronomical Society* **462** (2), 2256–2265, arXiv: <https://academic.oup.com/mnras/article-pdf/462/2/2256/8013538/stw1805.pdf>.
- HUGHES, D.W. & TOBIAS, S.M. 2001 On the instability of magnetohydrodynamic shear flows. *Proceedings of the Royal Society of London. Series A: Mathematical, Physical and Engineering Sciences* **457** (2010), 1365–1384, arXiv: <https://royalsocietypublishing.org/doi/pdf/10.1098/rspa.2000.0725>.
- JUN, BYUNG-IL, NORMAN, MICHAEL L. & STONE, JAMES M. 1995 A Numerical Study of Rayleigh–Taylor Instability in Magnetic Fluids. *The Astrophysical Journal* **453**, 332.
- KESKINEN, M. J., SZUSZCZEWICZ, E. P., OSSAKOW, S. L. & HOLMES, J. C. 1981 Nonlinear theory and

- experimental observations of the local collisional rayleigh-taylor instability in a descending equatorial spread f ionosphere. *Journal of Geophysical Research: Space Physics* **86** (A7), 5785–5792, arXiv: <https://agupubs.onlinelibrary.wiley.com/doi/pdf/10.1029/JA086iA07p05785>.
- KULKARNI, A. K. & ROMANOVA, M. M. 2008 Accretion to magnetized stars through the Rayleigh–Taylor instability: global 3D simulations. *Monthly Notices of the Royal Astronomical Society* **386** (2), 673–687, arXiv: <https://academic.oup.com/mnras/article-pdf/386/2/673/3607498/mnras0386-0673.pdf>.
- LINDEN, P. F. & REDONDO, J. M. 1991 Molecular mixing in Rayleigh–Taylor instability. Part I: Global mixing. *Physics of Fluids A: Fluid Dynamics* **3** (5), 1269–1277, arXiv: https://pubs.aip.org/aip/pof/article-pdf/3/5/1269/12749445/1269_1_online.pdf.
- MAK, J., GRIFFITHS, S. D. & HUGHES, D. W. 2017 Vortex disruption by magnetohydrodynamic feedback. *Phys. Rev. Fluids* **2**, 113701.
- OTT, EDWARD 1978 Theory of rayleigh-taylor bubbles in the equatorial ionosphere. *Journal of Geophysical Research: Space Physics* **83** (A5), 2066–2070, arXiv: <https://agupubs.onlinelibrary.wiley.com/doi/pdf/10.1029/JA083iA05p02066>.
- PRIEST, ERIC & FORBES, TERRY 2000 *Magnetic Reconnection: MHD Theory and Applications*. Cambridge University Press.
- RAMAPRABHU, P., DIMONTE, GUY & ANDREWS, M. J. 2005 A numerical study of the influence of initial perturbations on the turbulent rayleigh–taylor instability. *Journal of Fluid Mechanics* **536**, 285–319.
- RISTORCELLI, J. R. & CLARK, T. T. 2004 Rayleigh–taylor turbulence: self-similar analysis and direct numerical simulations. *Journal of Fluid Mechanics* **507**, 213–253.
- ROGERS, MICHAEL M. & MOSER, ROBERT D. 1992 The three-dimensional evolution of a plane mixing layer: the kelvin–helmholtz rollup. *Journal of Fluid Mechanics* **243**, 183–226.
- ROGERS, MICHAEL M & MOSER, ROBERT D 1994 Direct simulation of a self-similar turbulent mixing layer. *Physics of Fluids* **6** (2), 903–923.
- SCHILLING, OLEG 2020 A buoyancy–shear–drag-based turbulence model for rayleigh–taylor, reshocked richtmyer–meshkov, and kelvin–helmholtz mixing. *Physica D: Nonlinear Phenomena* **402**, 132238.
- SHEBALIN, JOHN V., MATTHAEUS, WILLIAM H. & MONTGOMERY, DAVID 1983 Anisotropy in mhd turbulence due to a mean magnetic field. *Journal of Plasma Physics* **29** (3), 525–547.
- SKOUTNEV, V., MOST, E. R., BHATTACHARJEE, A. & PHILIPPOV, A. A. 2021 Scaling of small-scale dynamo properties in the rayleigh–taylor instability. *The Astrophysical Journal* **921** (1), 75.
- SRINIVASAN, BHUVANA, DIMONTE, GUY & TANG, XIAN-ZHU 2012 Magnetic field generation in rayleigh-taylor unstable inertial confinement fusion plasmas. *Phys. Rev. Lett.* **108**, 165002.
- STONE, JAMES M. & GARDINER, THOMAS 2007a The magnetic rayleigh-taylor instability in three dimensions. *The Astrophysical Journal* **671** (2), 1726–1735.
- STONE, JAMES M. & GARDINER, THOMAS 2007b Nonlinear evolution of the magnetohydrodynamic rayleigh-taylor instability. *Physics of Fluids* **19** (9), 094104, arXiv: <https://doi.org/10.1063/1.2767666>.
- STRUTT, JOHN WILLIAM 2009 *Investigation of the Character of the Equilibrium of an Incompressible Heavy Fluid of Variable Density*, Cambridge Library Collection - Mathematics, vol. 2, p. 200–207. Cambridge University Press.
- SUCHANDRA, PRASOON & RANJAN, DEVESH 2023 Dynamics of multilayer rayleigh–taylor instability at moderately high atwood numbers. *Journal of Fluid Mechanics* **974**, A35.
- TAYLOR, GEOFFREY INGRAM 1950 The instability of liquid surfaces when accelerated in a direction perpendicular to their planes. i. *Proceedings of the Royal Society of London. Series A. Mathematical and Physical Sciences* **201** (1065), 192–196, arXiv: <https://royalsocietypublishing.org/doi/pdf/10.1098/rspa.1950.0052>.
- WEISS, NIGEL OSCAR & ADAMS, JOHN BERTRAM 1966 The expulsion of magnetic flux by eddies. *Proceedings of the Royal Society of London. Series A. Mathematical and Physical Sciences* **293** (1434), 310–328, arXiv: <https://royalsocietypublishing.org/doi/pdf/10.1098/rspa.1966.0173>.
- YOUNGS, DAVID L. 1991 Three-dimensional numerical simulation of turbulent mixing by Rayleigh–Taylor instability. *Physics of Fluids A: Fluid Dynamics* **3** (5), 1312–1320, arXiv: https://pubs.aip.org/aip/pof/article-pdf/3/5/1312/12749664/1312_1_online.pdf.
- YOUNGS, DAVID L. & THORNER, BEN 2020 Buoyancy–drag modelling of bubble and spike distances for single-shock richtmyer–meshkov mixing. *Physica D: Nonlinear Phenomena* **410**, 132517.
- ZHANG, H., BETTI, R., YAN, R., ZHAO, D., SHVARTS, D. & ALUIE, H. 2018 Self-similar multimode bubble-front evolution of the ablative rayleigh-taylor instability in two and three dimensions. *Phys. Rev. Lett.* **121**, 185002.
- ZHDANKIN, VLADIMIR, RIPPERDA, BART & PHILIPPOV, ALEXANDER A. 2023 Particle acceleration by magnetic

rayleigh-taylor instability: Mechanism for flares in black hole accretion flows. *Phys. Rev. Res.* **5**, 043023.

